AD-A171 353 NUMERICAL SIMULATIONS OF THE CELLULAR STRUCTURE OF DETONATIONS IN LIQUID..(U) NAVAL RESEARCH LAB WASHINGTON DC R GUIRGUIS ET AL. 31 JUL 86 NRL-MR-5810 F/G 19/4 NL

1/1

UNCLASSIFIED

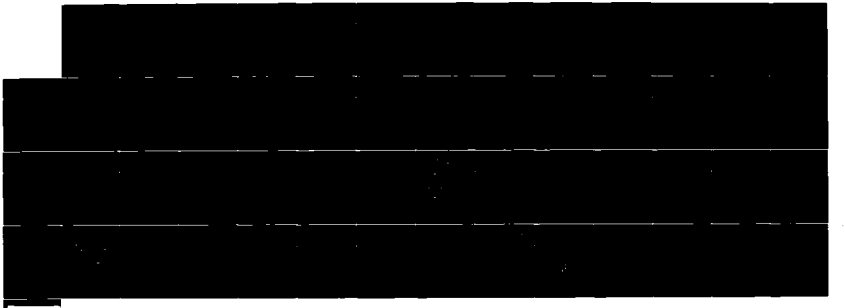

END
DATE FILMED
10-86
DTIC

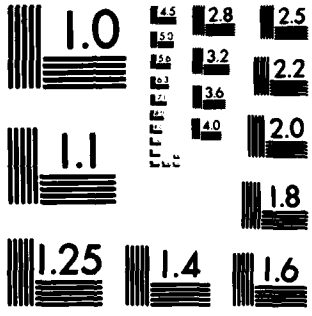

Naval Research Laboratory

Washington, DC 20375-5000 NRL Memorandum Report 5810 July 31, 1986

Numerical Simulations of the Cellular Structure of Detonations in Liquid Nitromethane—Regularity of the Cell Structure

R. GUIRGUIS,* E. S. ORAN, AND K. KAILASANATH

Laboratory for Computational Physics

**Berkeley Research Associates*
Springfield, VA 22150

SECURITY CLASSIFICATION OF THIS PAGE

AD-A171 353

REPORT DOCUMENTATION PAGE

1a. REPORT SECURITY CLASSIFICATION UNCLASSIFIED	1b. RESTRICTIVE MARKINGS
2a. SECURITY CLASSIFICATION AUTHORITY	3. DISTRIBUTION/AVAILABILITY OF REPORT
2b. DECLASSIFICATION/DOWNGRADING SCHEDULE	
4. PERFORMING ORGANIZATION REPORT NUMBER(S) NRL Memorandum Report 5810	5. MONITORING ORGANIZATION REPORT NUMBER(S)
6a. NAME OF PERFORMING ORGANIZATION Naval Research Laboratory 6b. OFFICE SYMBOL (If applicable)	7a. NAME OF MONITORING ORGANIZATION
6c. ADDRESS (City, State, and ZIP Code) Washington, DC 20375-5000	7b. ADDRESS (City, State, and ZIP Code)
8a. NAME OF FUNDING/SPONSORING ORGANIZATION Office of Naval Research 8b. OFFICE SYMBOL (If applicable)	9. PROCUREMENT INSTRUMENT IDENTIFICATION NUMBER
8c. ADDRESS (City, State, and ZIP Code) Arlington, VA 22217	10. SOURCE OF FUNDING NUMBERS PROGRAM ELEMENT NO.: 61153N, 61153N13 PROJECT NO.: 44-1528-0-6, 44-0313-A-6 TASK NO.: RR011-09-43, RR013-06-4R WORK UNIT ACCESSION NO: DN280-069

11. TITLE (Include Security Classification)
Numerical Simulations of the Cellular Structure of Detonations in Liquid Nitromethane—Regularity of the Cell Structure

12. PERSONAL AUTHOR(S)
R. Guirguis,* E. S. Oran, and K. Kailasanath

13a. TYPE OF REPORT	13b. TIME COVERED	14. DATE OF REPORT (Year, Month, Day)	15. PAGE COUNT
Memorandum	FROM _____ TO _____	1986 July 31	55

16. SUPPLEMENTARY NOTATION
*Berkeley Research Associate
Springfield, VA 22150

17. COSATI CODES			18. SUBJECT TERMS (Continue on reverse if necessary and identify by block number)
FIELD	GROUP	SUB-GROUP	Liquid nitromethane; Cellular structure; Regularity of cellular structure; Detonation

19. ABSTRACT (Continue on reverse if necessary and identify by block number)

The detailed structure of planar detonation waves in liquid nitromethane was studied using time-dependent two-dimensional numerical simulations. The walls are assumed to heavily confine the liquid explosive and boundary layer effects are neglected. The solution thus simulates the detonation structure near the center of a wide channel. Chemical decomposition of nitromethane is described by a two-step model composed of an induction time followed by energy release. A simplified equation of state based on the Walsh and Christian technique for condensed phases and the BKW equation of state for gas phases is used. When mixtures of both phases are present, pressure and temperature equilibrium between them is assumed. The simulations show a cellular pattern traced by a system of triple points dividing the detonation front into sections. However, a substructure of weaker triple points also trace out a non-uniform pattern within the main pattern, resulting in an irregular cellular structure. A correlation exists between the regularity of the cellular pattern and both the curvature of the front and the change in induction zone thickness at the triple points. If the induction time is a stronger function of temperature, the weaker triple points disappear and a more regular structure is produced.

(continues)

20. DISTRIBUTION/AVAILABILITY OF ABSTRACT	21. ABSTRACT SECURITY CLASSIFICATION
☒ UNCLASSIFIED/UNLIMITED ☐ SAME AS RPT. ☐ DTIC USERS	UNCLASSIFIED

22a. NAME OF RESPONSIBLE INDIVIDUAL	22b. TELEPHONE (Include Area Code)	22c. OFFICE SYMBOL
Elaine S. Oran	(202) 767-2960	Code 4040

DD FORM 1473, 84 MAR 83 APR edition may be used until exhausted. All other editions are obsolete.

SECURITY CLASSIFICATION OF THIS PAGE

19. ABSTRACT (Continued)

When the structures are regular, the detonation front is more curved and there is a larger change in induction zone thickness at the triple points. However, the large change in induction zone thickness also leads to the formation of unburned pockets that eventually disturb the symmetry and uniformity of the structure. We conclude that the regularity of the cellular pattern is strongly influenced by the temperature-dependence of the induction time.

CONTENTS

NUMERICAL SIMULATIONS OF THE CELLULAR STRUCTURE OF DETONATIONS IN LIQUID NITROMETHANE-REGULARITY OF THE CELL STRUCTURE

INTRODUCTION

Detonation waves were treated as steady, one-dimensional phenomena until 1926, when Campbell and Woodhead observed a spinning detonation front propagating in a round tube. This provided the first evidence that detonations are non-steady and have a local three-dimensional configuration. Since then, Manson, Edwards, Denisov and Troshin, Soloukhin, Strehlow, Oppenheim, Urtiew, and others, have carried out extensive experimental and theoretical studies of the structure of gas phase detonations. Some of the major findings of their work are summarized in the texts by Strehlow [1] and Fickett and Davis [2].

Numerical simulations of the detailed structure of detonation waves began around 1970. This delay occurred because such calculations require computers with large memory and algorithms with low inherent numerical diffusion to convect compressible flows where shocks might develop. The large amount of diffusion in early methods has the useful effect of smoothing out dispersion errors at discontinuities. However, it also smears out any transverse fluctuations, which caused the solutions to degenerate into the one-dimensional, steady Chapman-Jouguet solution. The first successful multi-dimensional numerical simulations of detonations, carried out by Taki and Fujiwara [3], showed that regardless of the details of the triggering disturbance, a fixed number of triple points is formed when a one-dimensional Chapman-Jouguet detonation is disturbed. Oran et al. [4], starting from a slightly oblique shock wave in a two-dimensional channel, produced a detonation front with a single triple point bouncing between the confining walls. Kailasanath et al. [5] investigated the problem of coupling with the confining walls and determined a natural size of the detonation cell width in a hydrogen-oxygen-argon mixture which agrees well with experimants.

Manuscript approved April 15, 1986.

The non-uniform nature of detonation waves in condensed phases was observed by Campbell et al. [6]. Shchelkin [7] suggested that detonations in condensed phases should exhibit the same structure as those in gases. Urtiew et al. [8] observed a criss-cross pattern of diagonal traces, similar to those inscribed on soot in gaseous detonations, indented on the side wall of a square channel in which a mixture of nitromethane and acetone was detonated.

There are definite similarities in the stuctures observed in the condensed and gas phases. However, condensed-phase detonations differ in two respects from gas-phase detonations. First, since the acoustic impedance of the walls is comparable to that of the condensed material they confine, the wall expands when a wave collides with it. The wall expansion generates rarefaction waves that weaken the detonation front and make it oblique to the wall. In addition, characteristic acoustic and chemical induction times are a few orders of magnitude less in condensed phases than in gases. As a result, the characteristic size of the detonation cells is considerably reduced.

In the present work we report the results of numerical simulations of the detailed structure of detonations in liquid nitromethane. Numerical simulations in condensed phases are particularly important since they can describe the structure of the detonation front in opaque materials for which optical diagnostics are difficult or impossible. The degree of numerical resolution required depends on the amount of numerical diffusion inherent in the finite-difference scheme used. In this work we have used a fourth-order Flux-Corrected Transport algorithm that can reproduce discontinuities with small dispersion errors and minimal numerical diffusion. Such an algorithm makes it possible to do two-dimensional calculations of compressible flows at reasonable costs in computer time and memory. We have considered the ideal case of a planar detonation propagating in a narrow slab of heavily-confined nitromethane. The problem modelled therefore simulates the configuration near the central axis of a wide tube, far from the locations where wall effects are important. Our objective is to show the formation and resulting configuration of multi-dimensional detonation structures in condensed phases, to get a preliminary estimate of a characteristic cell width, and to investigate the various factors controlling the regularity of the structure.

PHYSICAL MODEL

We have made the following assumptions:

1. The detonation is planar, and thus can be described by a two-dimensional model;
2. The normal component of velocity at the walls vanishes, while no restriction is imposed on the tangential velocity component;
3. The transformation of fuel to products is described by a two-step reaction model and occurs in the bulk of the condensed fuel; and
4. Within a small volume element, the condensed fuel and the gaseous products reach pressure and temperature equilibrium instantaneously.

Below we discuss the implications of these assumptions on our calculations.

When a detonation propagates in a rectangular or square tube, "transverse" waves move across the larger dimension (width) of the tube cross section, while "slapping" waves move across the normal direction (height). This three-dimensional configuration is called a "rectangular" detonation. If the slapping waves are suppressed, the front becomes cylindrical. This two-dimensional structure is called a "planar" detonation [1], which is the subject of this paper.

Since the acoustic impedance of a wall confining a condensed explosive is comparable to that of the explosive, the wall expands when a pressure wave collides with it. The wall expansion generates rarefaction "failure" waves that causes the detonation front to decay near the wall. Boundary layers also weaken the structure of the front near the wall. In our calculations, we assume that the normal velocity component at the wall vanishes. This is equivalent to assuming a perfectly rigid wall, known as "heavy confinement." We also impose no restriction on the tangential velocity component at the wall, and as a result boundary layers cannot form. This is known as "free slip." These two assumptions mean that the walls are perfect reflectors, and may be thought of as planes of symmetry in a channel many times wider. The resulting detonation structure

then models the structure found in the inner regions of a detonating explosive, far from the boundaries.

We have used a two-step reaction model to represent the transformation of fuel to products. The first step is a chemical induction period, in which

$$\text{Fuel} \longrightarrow \text{Radicals}, \qquad (\textit{step } 1)$$

while in the second step,

$$\text{Fuel} + \text{Radicals} \longrightarrow \text{Products}. \qquad (\textit{step } 2)$$

Since the fuel we are considering is a liquid, the transformation of fuel to gaseous products can occur in the gas phase, in the liquid phase, or at the interface between the two phases. For example, consider a small volume element containing both liquid fuel and gaseous products. Heat from the hot products could be transfered to the liquid surface causing evaporation of a thin layer of fuel, followed by both reaction steps occuring in the gas phase, away from the liquid surface. Alternatively, heat and radicals might diffuse from the products to the liquid surface where the second step occurs in the condensed phase. Finally, both reaction steps could occur in the bulk of compressed hot liquid in chemical and thermal isolation from the gaseous products.

The acoustic relaxation and chemical induction times in liquid nitromethane are much shorter than any diffusion time scale. We therefore neglect the effects of heat and radicals diffusion from the hot products to the liquid fuel surface, and assume that both reaction steps occur in the bulk of the liquid fuel. When a portion of fuel is converted to gaseous products, its sudden rise in pressure is communicated through pressure waves to the surrounding liquid. After pressure is equilibrated, the temperature of the adiabatically compressed neighboring liquid is generally lower than that of the expanded gases. However, the liquid reaches this temperature before any appreciable heating can occur by thermal conduction from the hot products. In addition, the chemical induction time is short in the range of temperatures achieved after this adiabatic compression. Thus the liquid fuel forms enough radicals within its bulk to start ignition, before any significant amount of radicals diffuse from the products to the liquid surface. In summary, we neglect the effects of surface chemical reactions.

During the chemical induction period, radicals are produced by step 1, an endothermic process, faster than they are consumed by step 2, an exothermic process. The concentration of radicals steadily increases but remains so small that the amount of fuel and energy consumed, and the amount of products produced during the induction period, can be neglected. The system temperature and the rate of step 1 remains nearly constant. As a result, the rate of step 1 can be expressed in terms of measured induction times, $\tau^o(T,\rho)$, while reaction step 2 can be assumed to start only after this induction time is elapsed. This is particularly useful when chemical kinetic rate data are not available. Induction times are measured at constant temperature, T, and density, ρ. Here, we use a superscript o to indicate that τ^o is a quasi-steady function of temperature, T, and density, ρ. If f denotes the fraction of induction time elapsed at time, t, then

$$\frac{df}{dt} = \frac{1}{\tau^o(T,\rho)} , \tag{1a}$$

where $f(0) = 0$, while the rate of step 2 remains zero until $f \geq 1$. If, within a small macroscopic volume element, each of the radicals can freely collide with any of the fuel molecules, the rate of step 2 would be proportional to the product of fuel and radicals concentrations. This is the case in gas phase reactions. In a condensed phase, however, the radicals produced are caged in the vicinity of their parent molecules, such that the radicals produced at one location cannot freely collide with distant fuel molecules. Therefore, we assume that the rate of fuel consumption can be expressed as

$$\frac{d}{dt}(\text{fuel mass}) = -(\text{fuelmass})Ae^{-E/RT}, \tag{2a}$$

once the radicals concentration reaches a critical level defined by $f = 1$. Under this assumption, f can be interpreted as the fraction of critical radical concentration per unit mass.

When the reaction occurs in a moving system, d/dt in Eqs. (1a) and (2a) denotes a substantial derivative that follows the system. Since the system mass is always conserved, if we denote by w the fraction of fuel mass in a mixture of fuel and products, Eq. (2a) can be written as

$$\frac{dw}{dt} = -wAe^{-E/RT}. \tag{2b}$$

For fuel, $w = 1$ yields a finite rate of fuel consumption once the value of f reaches 1. For products, $w = 0$ reduces the rate in Eq. (2b) to zero, thus ending the reaction process.

Using the continuity equation,

$$\frac{\partial \rho}{\partial t} + \frac{\partial \rho u}{\partial x} + \frac{\partial \rho v}{\partial y} = 0, \tag{3}$$

Eqs. (1a) and (2b) are rewritten as

$$\frac{\partial \rho f}{\partial t} + \frac{\partial \rho f u}{\partial x} + \frac{\partial \rho f v}{\partial y} = \frac{\rho}{\tau^o}, \tag{4a}$$

and

$$\frac{\partial \rho w}{\partial t} + \frac{\partial \rho w u}{\partial x} + \frac{\partial \rho w v}{\partial y} = -\rho w A e^{-E/RT}, \tag{5}$$

respectively. In the above equations, ρ denotes the total (fuel + products) density, while u and v denote the particle velocity components in the x and y directions. Equations (4a) and (5) describe the conservation of radicals and fuel, respectively. The left hand side of Eq. (4a) implies that, within a time interval dt, the radicals coming through the surfaces of a control volume $dxdy$ mix with the radicals inside, whether they were carried in by the liquid fuel or the gaseous products. We have assumed above, however, that the radicals in the gaseous products cannot diffuse quickly into the liquid and thus cannot contribute significantly to the reaction process. Equation (1a) is therefore rewritten as

$$\frac{d(fw)}{dt} = \frac{w}{\tau^o}, \tag{1b}$$

since w remains fixed at $w = 1$ during the induction time and dw/dt is independent of the radicals concentration f. Using Eq. (3), Eq. (1b) yields

$$\frac{\partial(\rho w f)}{\partial t} + \frac{\partial(\rho w f u)}{\partial x} + \frac{\partial(\rho w f v)}{\partial y} = \frac{\rho w}{\tau^o}, \tag{4b}$$

where only the radicals within the liquid fuel are mixed, since $w = 0$ for the products. Equation (4b) implies that some mixing occurs among radicals which are supposed to be caged in different portions of liquid fuel, a contradiction to the model assumptions. This mixing, however, vanishes as both dx and dy tend to zero, and is thus part of the discretization error.

Induction time measurements in liquid nitromethane were compiled by Chaiken [9], who expressed τ^o in an Arrhenius form, $A^o exp(E^o/RT)$. Of the different sets of data compiled, we selected those taken at Los Alamos National Laboratory, which gives $A^o = 2.3 \times 10^{-6}$ μs and $E^o = 29.1$ Kcal. The values of A and E in Eq. (2) were taken from Mader [10]: $A = 4.0 \times 10^8$ μs^{-1} and $E = 53.6$ Kcal.

Finally, we assume that within a small volume element, the liquid fuel and the gaseous products reach pressure and temperature equilibrium instantaneously. As explained above, after pressure equilibration within a small volume element, the temperature of the liquid fuel is generally lower than that of the gaseous products. However, in order to avoid the physical and numerical complications of solving a two-temperature problem, we assume thermal equilibrium between the two phases.

The set of conservation equations is completed by the momentum equations,

$$\frac{\partial(\rho u)}{\partial t} + \frac{\partial(\rho u u)}{\partial x} + \frac{\partial(\rho u v)}{\partial y} = -\frac{\partial p}{\partial x}, \tag{6a}$$

$$\frac{\partial(\rho v)}{\partial t} + \frac{\partial(\rho u v)}{\partial x} + \frac{\partial(\rho v v)}{\partial y} = -\frac{\partial p}{\partial y}, \tag{6b}$$

and the energy equation,

$$\frac{\partial E}{\partial t} + \frac{\partial(E u)}{\partial x} + \frac{\partial(E v)}{\partial y} = -\frac{\partial p u}{\partial x} - \frac{\partial p v}{\partial y}. \tag{7}$$

In Eq. (7), $E = \rho(e - (u^2 + v^2)/2)$, where e is the internal energy per unit mass and p is the pressure. The conservation relations are supplemented with the equation of state.

$$p = p(\rho, e, w)$$

and

$$T = T(\rho, e, w).$$

The HOM equations of state, described by Mader [10], are used for both condensed fuel and gaseous products. The equation of state for the condensed phase is based on the Christian and Walsh technique [11]. This technique requires measuring the relation between the shock velocity and particle velocity in the shocked material. A linear fit to the measurements is then solved simultaneously with the Hugoniot relations to derive the conditions behind the shock. States off the Hugoniot are related to those on it by using the Grüneisen $\gamma \equiv (\partial p/\partial e)|_\rho/\rho$, for the liquid.

The equation of state of the gaseous products is constructed by solving the equilibrium Chapman-Jouguet (CJ) detonation problem using the BKW equation of state for the final products. The equilibrium isentrope through the CJ point is evaluated and the states off the isentrope are derived using Grüneisen γ for the products. In those regions which contain a mixture of fuel and products, $0 < w < 1$, the specific volume and internal energy are subdivided between the two phases such as to yield the same pressure and temperature. The details of the equation of state and the iteration procedure required to satisfy temperature and pressure equilibrium are described by Guirguis, et al. [12].

NUMERICAL SOLUTION

Equations (3)–(7) are solved by operator splitting the fluid dynamics and the chemical reactions within the overall computational time step. For the fluid dynamics, Eqs. (3), (6a), (6b), (7) and the left hand sides of Eqs. (4b) and (5) are solved by splitting the $\partial/\partial x$ and $\partial/\partial y$ operators. Each is advanced using a fourth-order Flux-Corrected Transport (FCT) algorithm [13]. During the chemical step, the right hand side of Eq. (4b) is advanced using an explicit Euler method. When $f \geq 1$, indicating the end of the induction time, the right hand side of Eq. (5) is advanced using a fully-implicit Euler method.

In order to obtain the multi-dimensional structure of the detonation wave, the detailed structure of the induction zone has to be resolved. Otherwise, the solution degenerates into a one-dimensional steady configuration. In the multi-dimensional configuration, the shock front is divided by a system of triple points into alternating stronger, nearly-normal, Mach stems, and weaker, oblique, incident shocks. The reaction front follows the Mach stems closely, while the lower temperatures behind the incident waves yield induction zones extending beyond the reflected shocks, called here "transverse" shocks. In order to obtain the multi-dimensional configuration of the detonation wave, the resolution should be enough to distinguish the different sizes of the induction zones behind the Mach stem and incident shock. This requires keeping several computational grid points within the induction zone behind the incident waves.

To estimate the resolution required, one-dimensional calculations were used as a guide. It was found that for a nearly-steady one-dimensional detonation wave, the leading shock wave propagates at 0.68 cm/μs, while the temperature behind it is approximately 2700 K. The width of the induction zone, the difference between shock and particle velocities times the induction time, was found to be 2×10^{-4} cm. The particle velocity is evaluated from the shock velocity using the linear relation between

the two velocities described above in connection with the equation of state of liquid nitromethane.

In our two-dimensional calculations, the grid along the y-direction (the width of the channel) is kept fixed, with a uniform spacing of 4×10^{-5} cm. We used 75, 100, 125, and 150 computational cells along the y-direction giving computational domains 0.03, 0.04, 0.05, and 0.06 mm wide, respectively. The computational grid along the x-direction is composed of 200 cells, each initially 4×10^{-5} cm wide. When the shock front comes within 10 cells from the right boundary, the grid expands to guarantee a uniform spacing of 4×10^{-5} cm at all times around the shock and reaction zones. The result is that the shock front is locked within cell number 191. The resolution behind the induction zone smoothly decreases towards the left boundary. This type of grid motion, however, limits the time step to 1/3 the Courant time step, as explained below.

Denoting the local grid velocity by u_g, FCT guarantees positivity, provided

$$|u - u_g| \frac{\delta t}{\delta x} \leq 1/2, \tag{8}$$

which imposes an upper limit on both particle and grid displacements per time step. Let us assume

$$|u_g| \frac{\delta t}{\delta x} \leq \alpha.$$

The Courant condition for stability also imposes an upper limit on the particle displacement in a single time step. Let

$$(|u| + C) \frac{\delta t}{\delta x} \leq \beta \leq 1,$$

where C is the local sound speed [12]. The above equations have to be satisfied everywhere, and in particular at the shock front. Denoting the front velocity by U, $|u_g| \geq |U|$ at the shock front. This is required for the right boundary of the grid to be able to expand with the shock and can be satisfied, if we choose $\alpha \geq \beta$, since $|u| + C \geq |U|$

behind the shock front of a detonation wave. In addition, $|u| \leq C$ behind the shock front, yielding

$$|u|\frac{\delta t}{\delta x} \leq \frac{\beta}{2}.$$

Using the above inequalities, Eq. (8) gives

$$|u - u_g|\frac{\delta t}{\delta x} \leq |u|\frac{\delta t}{\delta x} + |u_g|\frac{\delta t}{\delta x} \leq \frac{1}{2}\beta + \alpha \leq \frac{1}{2}\alpha + \alpha = \frac{3}{2}\alpha$$
$$\leq \frac{1}{2}.$$

Hence $\alpha \leq 1/3$, and $\beta \leq \alpha \leq 1/3$. In our calculations, we select $(|u| + C)\delta t/\delta x \leq 1/4$, yielding an average time step 0.8×10^{-5} μs.

RESULTS

The calculations are performed in a two-dimensional domain representing a channel closed at one end. The channel is chosen to be approximately one detonation cell wide. The calculations start with a one-dimensional overdriven detonation which decays as it propagates. Before reaching Chapman-Jouguet conditions, a finite amount of energy is deposited into a rectangular pocket centered on the axis behind the shock-front. When the shock wave generated from the pocket reaches the detonation front, two transverse waves are formed, as illustrated by the pressure contours in Fig. 1. Figure 1 also shows the details of the interaction between the shock wave generated by the pocket and the rear wall. After a few collisions with the channel walls, the transverse waves establish the front structure.

The detonation cell width is estimated from the calculations by systematically varying the width of the channel. If the selected channel is too narrow, sonic waves have enough time to relax any transverse perturbations, and the solution degenerates to a one-dimensional detonation. On the other hand, if the channel is too wide, more than one detonation cell forms. If the channel is slightly smaller or larger than one cell width, the sections of the front near the walls intermittently change between one and multi-dimensional configurations [5]. To start the trial and error procedure, the cell width was assumed to be 30 times the induction zone thickness behind the one-dimensional detonation. This value was chosen by analogy to gas phase detonations, in which the detonation cell width is one to two orders of magnitude larger than the induction zone behind a one-dimensional Chapman-Jouguet detonation [1].

Figure 2 shows the pressure contours behind the detonation front as it propagates in a 0.06 mm wide channel. The pressure contours are plotted on equally scaled x and y axes. A heavy concentration of contours occurs at both shock and reaction fronts. The solid traces connecting the contours at different times represent the loci of the main triple points, defined as those points on the front at which the shock front sharply

changes its curvature. The set of solid traces define the main cellular pattern. The dashed traces define a secondary cellular pattern, inscribed by a set of secondary triple points. A secondary triple point causes a minor change in the shock front curvature and is mainly recognized by the transverse wave associated with it. The collection of solid and dashed traces exhibit an irregular cellular pattern. While transverse pressure waves are scattered behind those sections of the front that are nearly one-dimensional, they are localized at the points of change of curvature behind the most curved sections. When two transverse waves collide, a pair of triple points is formed. We note here that the secondary triple points appears to originate where the front is almost one-dimensional.

The sequence in Fig. 2 starts at time step 2500, where the main transverse waves have just reflected from the walls. At that time, the shock front is generally symmetrical. At step 3300, the front is asymmetrical, becoming nearly one-dimensional during steps 3600 to 4600. Disturbances behind the front form new triple points and at step 5500, the channel width is almost divided into two cells. Some of the structure regularity and symmetry is regained at step 6000. However, during steps 6000 to 6600, the front becomes again nearly one-dimensional, and the same behavior is repeated. The pattern traced by the triple points alternately divide the channel width into one or two cells.

Figures 3a and 3b show the details of the evolution of the detonation structure between time steps 5000-6000 and 7500-8200, when the width of the channel is divided into two cells. In these two figures the individual contours are not separated to scale, so that the solid and dashed traces merely connect the triple points. These traces are used to show the origin of the triple points and how they evolve. Again, triple points are mainly recognized by changes in the curvature of the front and by the transverse waves associated with them.

The temperature contours illustrated in Figs. 4a and 4b provide an alternative approach to locating the triple points. The reaction front is well defined on the temperature contours. When the temperature behind the shock front is below the selected minimum contour level, the shock front does not show on the contours. This appears in the figures as large gaps at the front. The region confined between the shock and reaction front is the induction zone. At a triple point, there is a change in induction zone thickness and a slip line originates. The stonger the triple point, the sharper the slip line appears and the larger the change in induction zone thickness. The strength of a triple point is defined as the pressure ratio across the transverse wave. At steps 3200 and 3300, in Fig. 4a, two triple points are colliding. We notice the sudden change in induction zone at the point of collision as well as the two slanted slip lines. We can also barely distinguish two transverse shocks, nearly parallel to the center line of the channel. Later on, at step 3900, we can distinguish two intersecting slip lines originating from the two triple points now travelling towards the walls. However, the change in induction zone thickness in this case appears to be of the same order of magnitude as the change caused by the disturbances behind the shock front. As will be explained later, this is one of the main reasons for the irregularity of the cell structure. Finally, at step 5100, both the slip lines and the changes in induction zone are barely defined, although we can distinguish the transverse shocks associated with the two triple points, now travelling toward the center of the channel.

The temperature contours in Fig. 4b show a set of pressure waves and slip lines dividing the field behind the detonation wave into many regions. The two triple points near the center are in the process of colliding, while those two near the walls have already collided. We can distinguish two transverse shocks emanating from the two triple points near the center and four slip lines. Following the sequence from step 7600 to 7900, we see one of the transverse shocks interact with a slip line. The main interaction occurs at step 7800. Again, the change in induction zone thickness at the triple points is barely noticeable except when two triple points are colliding.

Figures 5 and 6 show the pressure contours near the propagating detonation front for two channel widths, 0.05 and 0.04 mm, respectively. Again, the solid traces represent the loci of the main triple points, the dashed traces define a secondary cellular pattern, and the collection of these lines exhibit an irregular cellular pattern.

In Fig. 5, most of the secondary triple points are formed between steps 2400 and 2800, when the front is nearly one-dimensional. The main cellular pattern is quite symmetrical. Starting from step 4600, the channel width is divided into two clearly defined main cells. In addition to two triple points near the center at step 4600, we see a third main triple point near the top wall where there is a change of the front curvature. This also occurs at step 4900, near the bottom wall.

In Fig. 6, the detonation front is nearly one-dimensional between steps 2100 to 2900. During this period, the main triple points weaken and eventually become secondary triple points, while three secondary triple points strengthen and become main ones. As a result, the main cellular pattern becomes skewed, composed of one main cell reflecting up and down between the two walls. At step 4500, this cell width measures approximately 0.03 mm.

The later steps in Figs. 2, 5, and 6 show the system of triple points dividing the width of the channel into more than one cell, each approximately 0.03 mm wide. However, the irregular cellular pattern is not a transient in the process of establishing a cell width of 0.03 mm. This is verified by the calculations shown in Fig. 7, which illustrates the structure of the detonation front as it propagates into a channel 0.03 mm wide. Here again the first transverse waves are produced by depositing a finite amount of energy into a rectangular pocket centered on the axis behind the shock-front of the initially one-dimensional detonation. Two triple points are thus formed. However, after a transient period, a structure is formed at the detonation front which has only one main triple point that bounces between the two walls. This is shown starting from step 5800 in Fig. 7. This triple point traces a pattern equivalent to half a detonation cell. Since the walls are perfect reflectors, we would expect to observe one clearly defined

full cell when the channel width is doubled. This is not observed however in a channel 0.06 mm wide, as shown by Fig. 2. We conclude that the patterns observed in Fig. 2, 5, and 6, are indeed irregular structures, not just a transient behavior.

STABILITY OF THE MULTI-DIMENSIONAL STRUCTURE

The formation of the multi-dimensional structure of a detonation front can be understood by considering the effects of fluctuations on a homogeneously heated reactive material. Fluctuations in density or temperature, which always exist, give rise to local hot regions. In energetic materials, the chemical induction time is strongly dependent on temperature. Once a hot spot is formed, it ignites before the surrounding medium ignites. Compression waves then propagate the resulting local rise in pressure in all directions. Because of the heating associated with compression, these waves accelerate the chemical reaction in neighboring regions. In turn, these regions ignite and generate more compression waves. Moreover, when the pressure waves generated from other hot spots interact at some location with the first set of waves, they create new hot spots there. A general conclusion is that truly homogeneous combustion cannot persist in a reactive material in which the induction time is a strong function of temperature.

The existence of a one-dimensional detonation wave implies homogeneous combustion in the transverse direction behind the leading shock front. Since such homogeneity cannot persist when the system is perturbed, the one-dimensional configuration is unstable to transverse perturbations. Erpenbeck [14] has shown that if the exothermic kinetics of a system are strongly dependent on temperature, one-dimensional detonation waves are linearly unstable to transverse perturbations. However, the linear analysis cannot tell us what the final configuration must be.

When perturbed, the detonation evolves into a dynamically stable configuration, a repeatable, organized structure conforming to the geometry of the boundaries or symmetry planes. The transverse direction is divided by a system of triple points into alternating hotter and colder regions. The regions behind the nearly normal Mach stems are hotter. Those confined between the incident and transverse sections of the front are colder. This configuration is stable because the induction time of the colder regions is too long for fluctuations to start ignition. The colder regions do not ignite until the

transverse waves, themselves small detonations propagating in the transverse direction. consume them. As the detonation propagates, the triple points trace a cellular pattern called "cellular structure."

The multi-dimensional configuration described above is not always stable, thus not always repeatable. As explained above, one-dimensional detonations cannot persist. As a result, if a section of the front becomes nearly one-dimensional, the disturbances behind the shock front coalesce into two or more transverse waves. When these waves interact, secondary triple points are formed, leading to the irregular structures presented above. The results also show that while transverse waves are scattered behind those sections of the front that are nearly one-dimensional, they are localized near the triple points behind the curved sections. We can conclude thus that the sharper the curvature of the front between the triple points, the more stable it is. We then ask: what is the meaning of increasing the curvature of the front, and which properties of the system control it?

As explained above, the multi-dimensional structure is stable because the colder region behind an incident wave does not ignite until the reaction front, coming from the hotter region behind the Mach stem, consumes it. The temperature contours at steps 3900 and 5100, Fig. 4a, show that the change in induction zone at the triple points is of the same order of magnitude as the changes caused by perturbations behind the shock front. This observation suggests that the difference in induction times, corresponding to the difference in temperatures behind the Mach stems and incident waves, may not be enough to yield a stable detonation structure. If the change in induction zone thickness at the triple points were much larger than any possible change due to perturbations behind the shock, the multi-dimensional structure could become stable. Below we show that this hypothesis is correct. We make the multi-dimensional structure more stable by increasing the induction time behind the incident shocks, the colder regions, while decreasing the induction time behind the Mach stems, the hotter regions.

Consider Fig. 8, which shows the Arrhenius line 0, the logarithm of the induction time and reciprocal of temperature. The horizontal line, included for reference, corresponds to the hypothetical case in which the induction time is independent of temperature. In this case, a hot spot does not ignite any faster than the surroundings. This makes homogeneous combustion and in turn one-dimensional detonations possible. We rotate the induction line to position 1 which is 50% steeper. In order to keep the detonation cell width roughly fixed, we rotate the induction line about a point on the line corresponding to the temperature behind the shock wave of the one-dimensional Chapman-Jouguet (CJ) detonation. Here we assume that, as in gas phase detonations, the cell width is proportional to the induction zone thickness of the one-dimensional CJ detonation. In addition, the temperature behind the shock of the one dimensional detonation should be somewhere in between the minimum temperature reached behind the Mach stem and the maximum temperature reached behind the incident shock. These temperatures change across the transverse direction, as the detonation propagates through one cycle (half a cell length), and from one cycle to the next. Rotating the induction line is thus equivalent to making the induction times behind the Mach stems shorter and behind the incident waves longer. In an experiment, this could accomplished by mixing the nitromethane with another liquid such as to make the induction time a more sensitive function of temperature.

Figure 9 illustrates the pressure contours behind the detonation front when the induction time is described by line 1 in Fig. 8. Line 1 is obtained by rotating line 0 about 2700 K, the temperature behind the shock of the one-dimensional detonation, to a 50% larger slope. Then $A^o = 1.55 \times 10^{-7}$ μs and $E^o = 43.65$ Kcal. All other parameters are the same as in the case of Fig. 5. Comparing Figs. 9 and 5 shows that the detonation structure has become much more regular as a result of the change in temperature dependence of the induction time. The curvature of the shock front and the two main triple points are sharply defined throughout the whole sequence. We do not observe any secondary triple points. The structure is symmetrical.

The details of the structure are shown on the pressure and temperature contours in Figs. 10a and 10b. On the pressure contours, the transverse shocks are sharply defined, while a reaction front appears as a spotted stripe. The temperature contours are heavily concentrated at the reaction front. On the temperature contours, the slip lines are sharply defined while the transverse shocks are barely distinguishable. We notice the change in induction zone thickness near the triple points.

First consider the pressure contours of Fig. 10a. The sequence starts at step 2100, when the two triple points have just reflected from the walls. During steps 2100 to 2900, the triple points travel from the walls to the center of the channel. As the transverse shocks interact, from step 2600 to step 2900, their inclination to the center line changes. The curvature of the shock-front is reversed, and the Mach stem and incident shock switch roles. (The incident wave is the section of the front that is squeezed between the transverse waves). The reaction front follows the Mach stem closely, but is far from the incident shock. On the temperature contours, two unreacted pockets of material appear near the wall starting from step 2400. These appear because of the formation of a second reaction front behind the incipient Mach stem, better illustrated in Fig. 10b. Finally, the contours of step 2100 are similar to those of step 2900, except for an upward or downward displacement equal to half the width of the channel. The sequence, steps 2100 to 2900, describe one cycle of the structure, during which the front propagates through half a cell length.

The sequence in Fig. 10b begins at a time just after the transverse shocks have collided and reflected from each other at the center, and are now propagating towards the walls. As they interact with the walls around step 3700, they change their inclination, and by step 3900 the transverse shocks propagate back towards the center. A second reaction front forms between steps 3000 and 3300 at the center, just behind the Mach stem, as shown by the temperature contours. As the two reaction fronts consume the material between them, a pocket of unburned material is isolated at the center. Small pockets of unburned material should not affect the regularity of the

structure. Large pockets, however, cause a significant energy-release deficit behind the detonation, which eventually disturbs the regularity of the structure. The formation of unreacted pockets has been observed both in experiments and numerical simulations of gas phase detonations [5,15]. Steps 2900 to 3900 describe a sequence slightly longer than one cycle. The contours of steps 2900 and 3900 are almost similar, except for an upward or downward displacement equal to half the width of the channel.

Finally, Figs. 10a and 10b show a phase lag between the shock front and the reaction front cycles. The transverse shocks always originate at the triple points, where the shock front suddenly changes its curvature. However, the local changes in the location of the reaction front always lag behind the local changes in the curvature of the shock front. For example, at step 2400, the reaction front at the center is as close to the incident shock as it is to the Mach stem near the wall. The reaction front does not fall far behind the incident shock, as is expected, until step 2900. At step 2900, the reaction front is ahead of the propagating transverse wave. The transverse wave does not move ahead of the reaction front until step 3300. This phase lag corresponds to a finite induction time, since the reaction occurs because of the shock heating.

EFFECTS OF INDUCTION TIME PARAMETERS

We have shown in the previous section that the regularity of the multi-dimensional structure can be improved by making the induction time a stronger function of temperature. This was accomplished by rotating the Arrhenius line 0 to line 1 in Fig. 8 about a point on the line corresponding to the temperature behind the shock front of a one-dimensional detonation. However, rotating the line also resulted in the formation of large unreacted pockets that eventually distorted the front structure again. Below we investigate the effects of rotating the induction line by different amounts and about different temperatures.

Figure 11 shows the results when the induction line is rotated about 2700 K to become 20% steeper, yielding $A^\circ = 7.83 \times 10^{-7}$ μs, and $E^\circ = 34.92$ Kcal. Again, all other parameters are the same as those used in the calculations shown in Fig. 5. The curvature of the front is not as pronounced, and the structure is not as symmetrical as in the case of 50% rotation illustrated in Figs. 10. The temperature contours do not show the same change in induction zone thickness at the triple points, except when the two transverse waves collide. Since the 20% case combines some of the features of both the irregular and regular structures, it was chosen to test the convergence of the numerical simulations.

Figures 12a and 12b demonstrate the convergence of the numerical calculations. The results on the left were obtained by limiting the time step to 0.25 the Courant time step. The results on the right corresponds to the case when the time step was limited to 0.125 the Courant time step. The initial conditions of the second calculations were taken as the results of step 2100, from the first calculation. The results are compared at nearly equal times. Figure 12a and 12b show the comparison of the pressure and temperature contours, respectively.

The effect of rotating the induction line to become 50% steeper, but about different temperatures, is illustrated in Figs. 13 and 14. This is equivalent to a combination of

rotating the induction line about 2700 K, and a parallel displacement to shorten or lengthen the induction time at all temperatures. This is illustrated by lines 2 and 3 in Fig. 8. All other parameters are kept the same as in the case of Fig. 2. Figure 13 shows the result of rotating the induction line 0 about 2400 K to line 2, in which case $A^o = 1.11 \times 10^{-7}$ μs and $E^o = 43.65$ Kcal. the resulting induction times are shorter than those corresponding to rotation about 2700 K. The induction zone is thinner, thus reducing the overall change at the triple points. The curvature of the front is much less than those curvatures observed in Figs. 10, and the structure not as symmetrical. In addition, the cell appears to be smaller than the channel width.

The results of rotating the induction line about 2800 K to become 50% steeper are shown in Figs. 14. In this case $A^o = 1.71 \times 10^{-7}$ μs and $E^o = 43.65$ Kcal, denoted as line 3 on Fig. 8. The resulting induction times are slightly longer than those corresponding to rotation about 2700 K. The induction zone is thicker, thus giving a larger change in induction zone thickness at the triple points. Such a large induction zone increases the tendency to form unburned pockets, as illustrated by the sequence of temperature contours in Fig. 14a. At step 1500, following collision of the triple points at the center, a second reaction front is formed behind the new Mach stem. As a consequence, a pocket of unreacted material is isolated at step 1700. The pressure contours in Fig. 14b exhibit as sharp a curvature of the front, as in the case of rotation about 2700 K shown in Figs. 10. However, because the unburned pocket holds energy and releases it later, the transverse shocks are slightly dispersed and the structure is not completely symmetrical. In addition, two new large pockets form near the wall. This is shown in the temperature contours starting from step 3100.

As a compromise between a large change of induction zone at the triple point and the tendency to form unburned pockets, Figs. 15a and 15b show the results of rotating the induction line to become only 30% steeper, about a point on the line corresponding to 2700 K. In this case, $A^o = 4.57 \times 10^{-7}$ μs and $E^o = 37.83$ Kcal. All other parameters in the calculation are the same as those used in the calculation

shown in Fig. 5. Figure 15a shows in detail the process of collision of the triple points with the walls, while Fig. 15b shows the details of collision at the center of the channel. Since the walls are perfect reflectors, these two processes should be similar provided the structure is stable in the sense that it is repeatable from cycle to cycle. The change in induction zone at the triple points is not as large as in the case of the 50% steeper induction line shown in Figs. 10. However, no large unburned pockets are formed. Thus although the curvature of the front is not as pronounced, the structure remains symmetrical and the transverse shocks are sharply defined at all times. We can clearly distinguish the slip lines originating at the triple points on the temperature contours. Finally, the repetition from cycle to cycle is improved. Contours which are 1000 steps apart are very similar, differing only by an upward or downward displacement equal to half the channel width.

DISCUSSION AND CONCLUSIONS

We have used time-dependent two-dimensional numerical simulations to study the detailed structure of planar detonation waves in liquid nitromethane. To calculate the multi-dimensional structure of the front, a fourth-order Flux-Corrected Transport (FCT) algorithm was used for convection. In addition, it was necessary to resolve the reaction zone with a number of grid points. Convergence was achieved using 4×10^{-5} cm computational cells and an average time step of 0.8×10^{-5} μs.

Since we have neglected the boundary layer effects and have assumed rigid walls, the simulation models the inner region of a large slab of material. Failure waves, originating when the wall expands, and boundary layers distort the structure of the detonation front and those cells near the wall. Since a typical detonation cell in liquid nitromethane is about 0.05 mm, any practical system is at least 20 to a 100 cells wide. The inner region of such a system is expected to contain a large number of cells for which the wall effects are insignificant and therefore can be described by heavy confinement.

The simulations show that when the one-dimensional detonation front is perturbed, it evolves into a system of colliding triple points that trace a cellular pattern. In pure liquid nitromethane, the resulting cellular pattern is irregular. The width of a detonation cell is approximately 0.05 mm. It is important to note however that the accuracy of this estimate is contingent on how accurately the equation of state and chemistry are represented.

The equation of state has been extensively used in the past. In one-dimensional systems it gave results reasonably close to experimental observations [10]. The two-step reaction chemistry model that we used is based on parameters obtained from direct measurements of the induction times in liquid nitromethane. Since the induction time plays the major role in forming the cellular structure, a simple model that uses directly measured induction times should be superior to any detailed chemical kinetics model in which the reactions rates are at best a very rough guess.

Experimental observations of the cellular structure in liquid nitromethane were carried out using mixtures of nitromethane and acetone [1,2,8], thus the observed detonation cells size cannot be directly compared to the model predictions. However, the cellular structures observed in mixtures of nitromethane and acetone are irregular, which is consistent with the model predictions.

The calculations of the irregular structures showed a correlation between the curvature of the front and generation of disturbances that caused the irregularity. As a detonation propagates, its front often becomes nearly one-dimensional. The simulations then show weak transverse pressure waves scattered behind the flat sections of the front. Coalescence of two or more of these waves then generates the secondary triple points that cause the non-uniform pattern. In contrast to this, the transverse pressure waves are relatively localized at the points of change of curvature behind the highly curved sections of the front. We conclude that highly curved detonation fronts lead to more regular patterns.

The calculations of the irregular structure also show that the change in the thickness of the induction zone at the triple points is of the same order of magnitude as the changes caused by the tranverse waves scattered behind the front. This led us to the hypothesis that the structures would be more regular if the change in induction zone thickness at the triple point were made larger than any changes caused by perturbations behind the front. This was verified by changing the induction time so that it became a stonger function of temperature, and repeating the calculations. A stronger function means a larger change in induction time for a given change in temperature.

The degree of regularity of the detonation cell structure is sensitive to the temperature dependence of the induction time. This was shown by rotating the Arrhenius line (the relation between the logarithm of the induction time and reciprocal of temperature, Fig. 8) to various slopes and about various points on the line. The most regular structure was obtained when the Arrhenius line was made 30% steeper and was rotated about a point corresponding to the temperature behind the shock front of the

one-dimensional detonation. Smaller slopes did not produce stable multi-dimesional structures. Larger slopes resulted in the formation of large pockets of unreacted material, which eventually distorted the symmetry and uniformity of the structure from one detonation cell to the next. In general, the calculations in which the induction line was rotated about a lower temperature showed an irregular structure. Those in which the induction line was rotated about a higher temperature showed a greater tendency to form pockets of unreacted material.

When the calculations showed a regular cellular structure, we did not see the weak triple points that formed the cellular substructure in the irregular cases. Only sharply defined triple points traced the cellular pattern. The curvature of the front was also sharply defined at all times. The change in induction zone thickness at the triple points was much larger than any changes caused by disturbances behind the front. However, even when the structure was regular it is not nearly as repeatable as those patterns observed and calculated for H_2–O_2 mixtures highly diluted in argon [5].

Finally, it is important to note that in the liquid nitromethane system we have studied, the chemical induction time is much longer than the energy release time. Specifically, the induction time is one order of magnitude larger than the energy release time at 2700 K, the temperature behind the shock front of the one-dimensional detonation. Future work should include parametric studies of other effects such as energy release process and the equation of state on the regularity of the cellular structure. It is important to investigate the effects of having a channel width which is two detonation cells or wider. Another important approach is to calculate the cellular structure in H_2–O_2 mixtures without any dilution. Kailasanath, et al. [5] obtained highly regular structures for mixtures of H_2–O_2 diluted in argon. From what we have now learned, we expect to see irregular structures in H_2–O_2 mixtures if no argon is present.

ACKNOWLEDGEMENT

This work was supported by the Naval Research Laboratory, Special Focus Program on Controlled Energy Release, through the Office of Naval Research. The authors would like to acknowledge the help of Dr. J.P. Boris and the information provided by Dr. R.F. Chaiken.

REFERENCES

1. Strehlow, R.A., *Fundamentals of Combustion*, Krieger Publishing Co. (1979); also *Combustion Fundamentals*, M McGraw Hill (1984).
2. Fickett, W. and Davis, W.C., *Detonation*, University of Califfornia Press (1979).
3. Taki, S. and Fujiwara, T., *AIAA* 76:404 (1976).
4. Oran, E.S., Boris, J.P., Young, T., Flanigan, M., Burks, T., and Picone, M., *Eighteenth Symposium (International) on Combustion*, The Combustion Institute, Pittsburgh, 1981, p. 1641.
5. Kailasanath, K., Oran, E.S., Boris, J.P., and Young, T.R., *Comb. Flame* 61:199 (1985).
6. Campbell, A.W., Holland, T.E., Malin, M.E., and Cotter, T.P., *Nature* 178:38 (1956).
7. Shchelkin, K.I., *Zh. Eksperim. i Teor. Fiz.* 36:600 (1959).
8. Urtiew, P.A., Kusubov, A.S., and Duff, R.E., *Comb. Flame* 4:117 (1970).
9. Chaiken, R.F., *Behavior of Dense Media Under High Dynamic Pressure*, Proceedings of the High Dynamic Pressure Symposium held in Paris, France, Aug. 27 - 31, 1978, Commissariat d'Energie Atomique, Paris, France.
10. Mader, C.L., *Numerical Modeling of Detonations*, University of California Press (1979).
11. Walsh, J.M. and Christian, R.H., *Phys. Rev.* 97:1544 (1955).
12. Guirguis, R. and Oran, E., *Reactive Shock Phenomena in Condensed Materials: Formulation of the Problem and Method of Solution* NRL Memo. Rep. 5228, Naval Research Laboratory, Washington, D.C. 20375 (1983).
13. Boris, J.P., *Flux-Corrected Transport Modules for Solving Generalized Continuity Equations*, NRL Memo. Rep. 3237, Naval Research Laboratory, Washington, D.C. 20375 (1976).
14. Erpenbeck, J.J., *Phys. Fluids* 7:684 (1964).
15. Oran, E.S., Young, T.R., Boris, J.P., Picone, J.M., and Edwards, D.H., *Nineteenth Symposium (International) on Combustion*, The Combustion Institute, 1982, p.573.

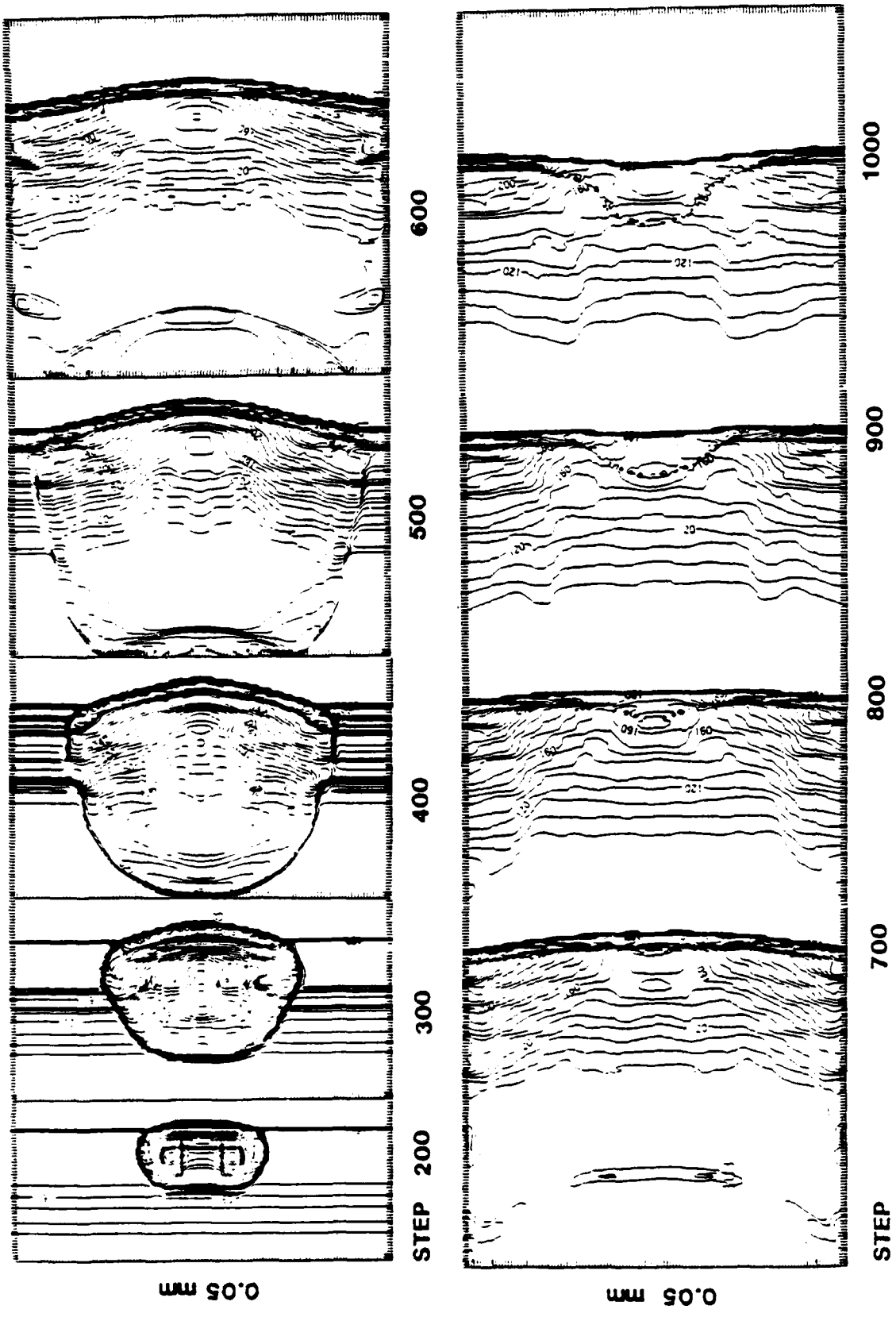

Fig. 1 — Pressure contours of a typical initiation of the multi-dimensional detonation structure.

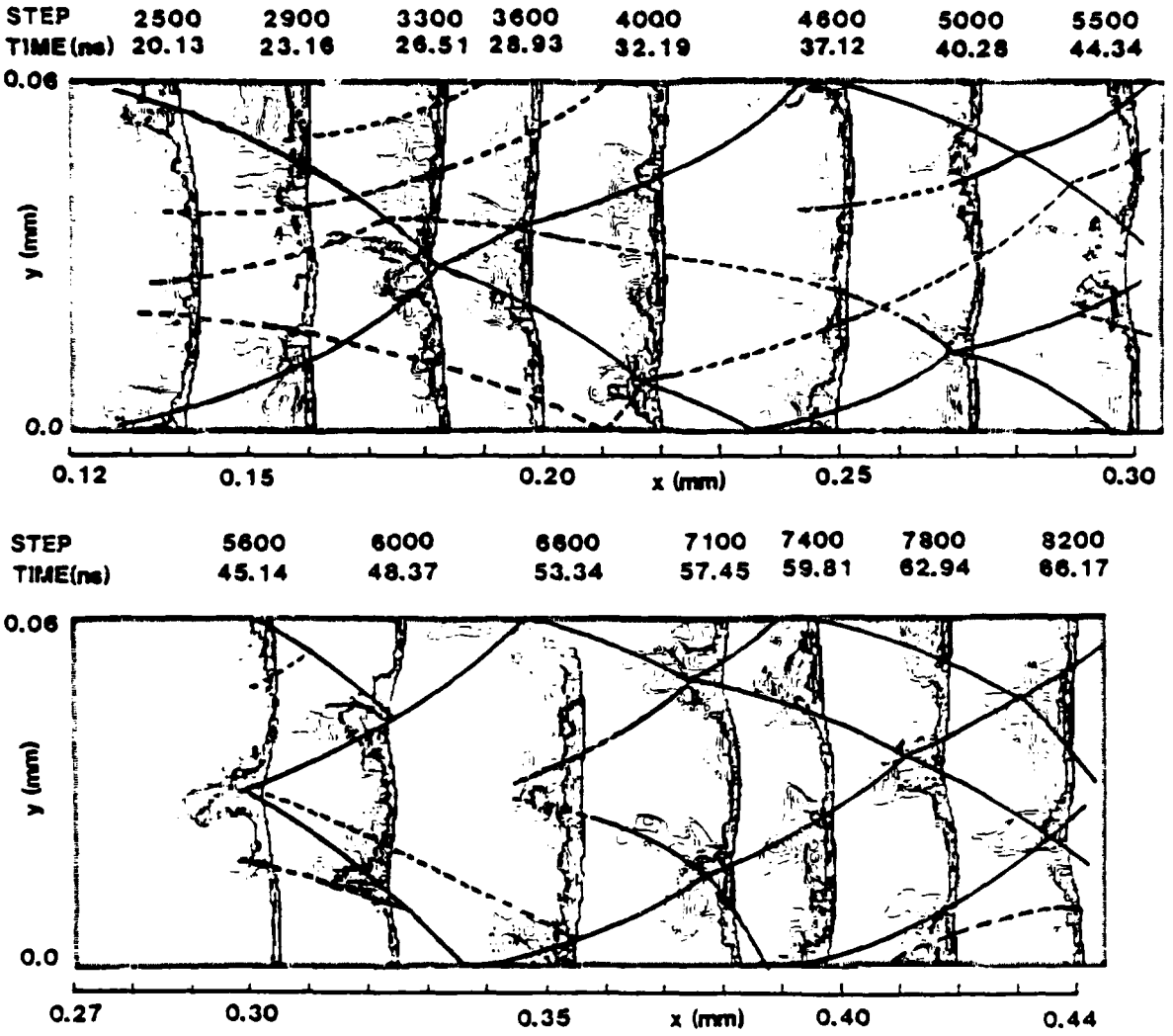

Fig. 2 — Pressure contours of a detonation wave propagating in a channel 0.06 mm wide. Solid traces are loci of main triple points. Dashed traces are loci of secondary triple points.

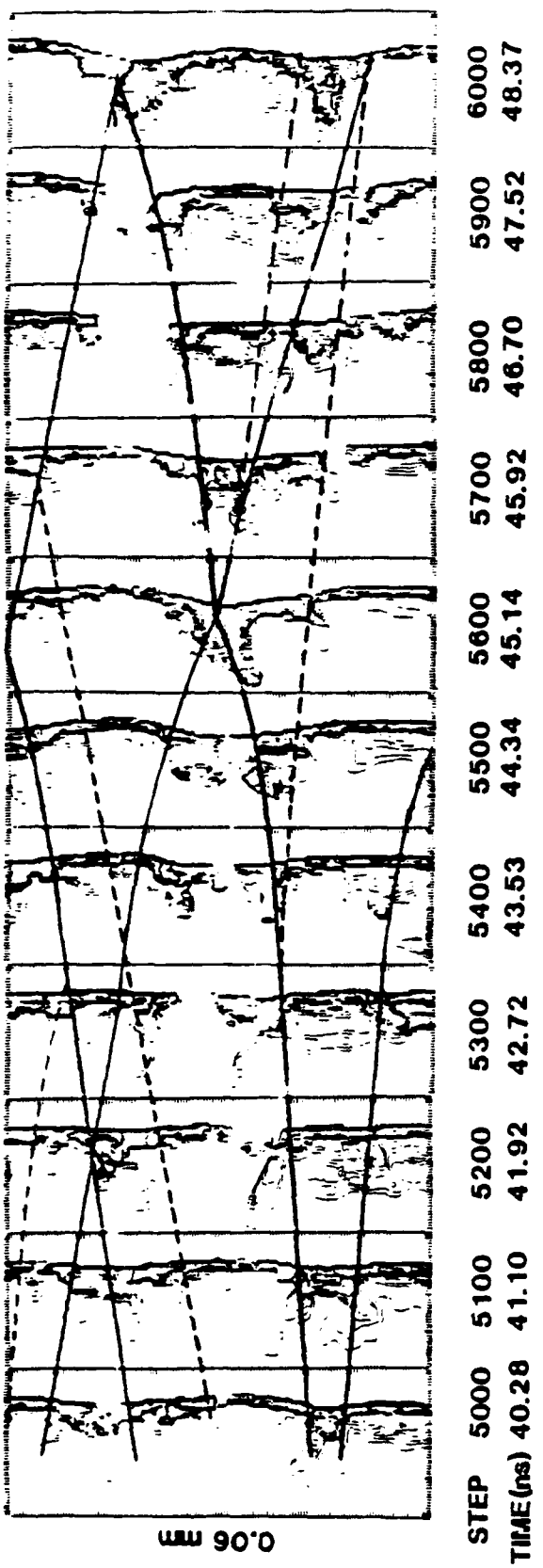

(a)

Fig. 3 — Pressure contours of detailed evolution of structure of the detonation front in Fig. 2 between time steps (a) 5000-6000 and (b) 7500-8200.

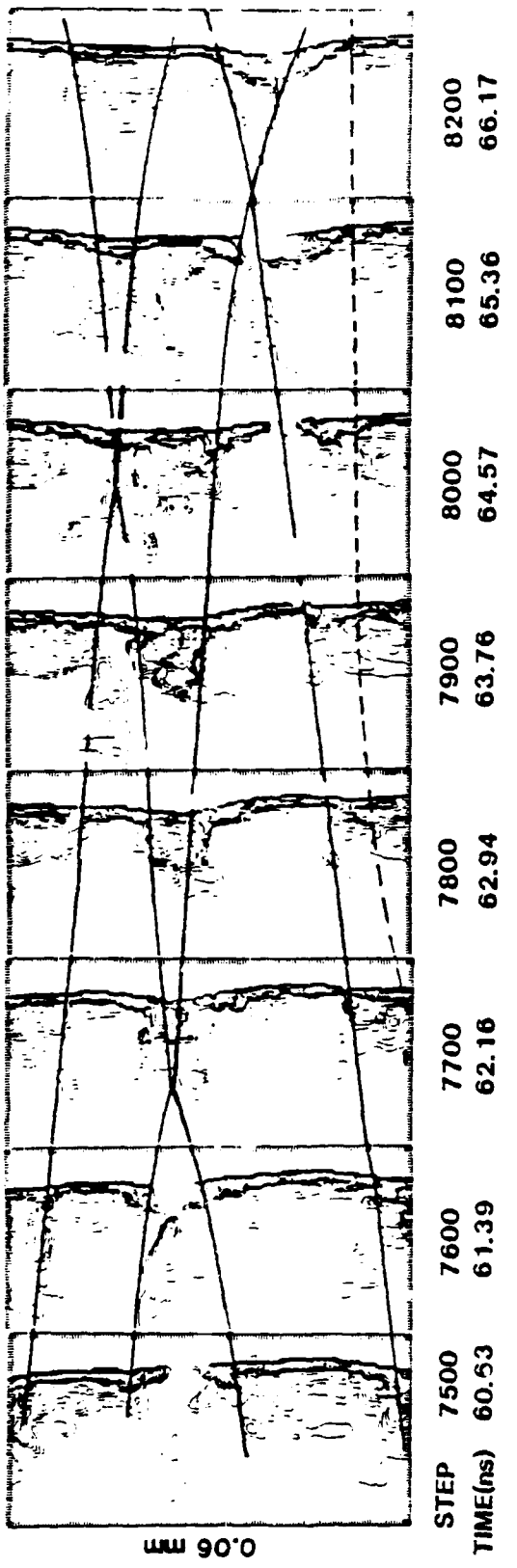

(b)

Fig. 3 (Continued) — Pressure contours of detailed evolution of structure of the detonation front in Fig. 2 between time steps (a) 5000-6000 and (b) 7500-8200.

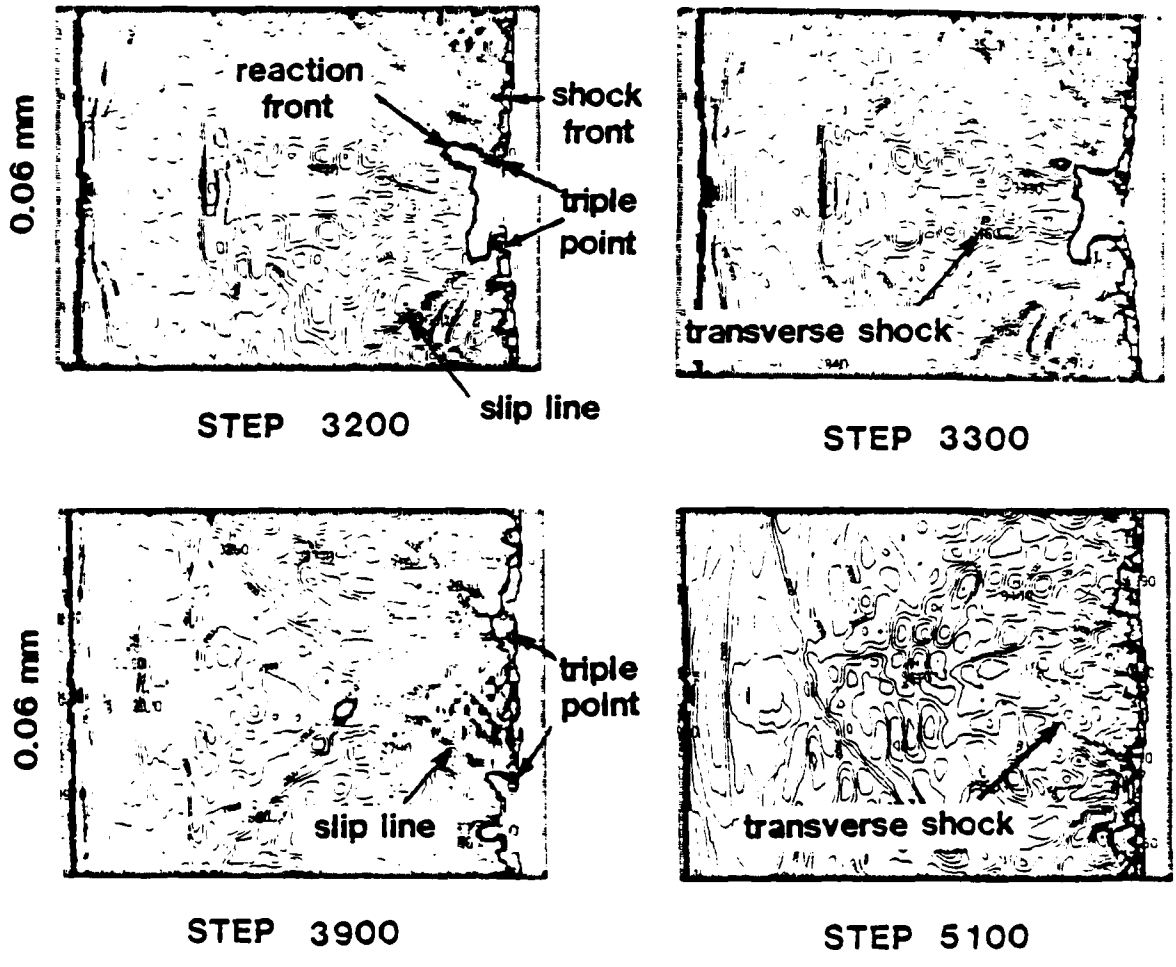

(a)

Fig. 4 — Temperature contours behind the detonation wave in Fig. 2. The induction zone is the region in between the leading shock front and the reaction front. (a) Two main triple points divide the channel width; (b) Four main triple points divide the channel width.

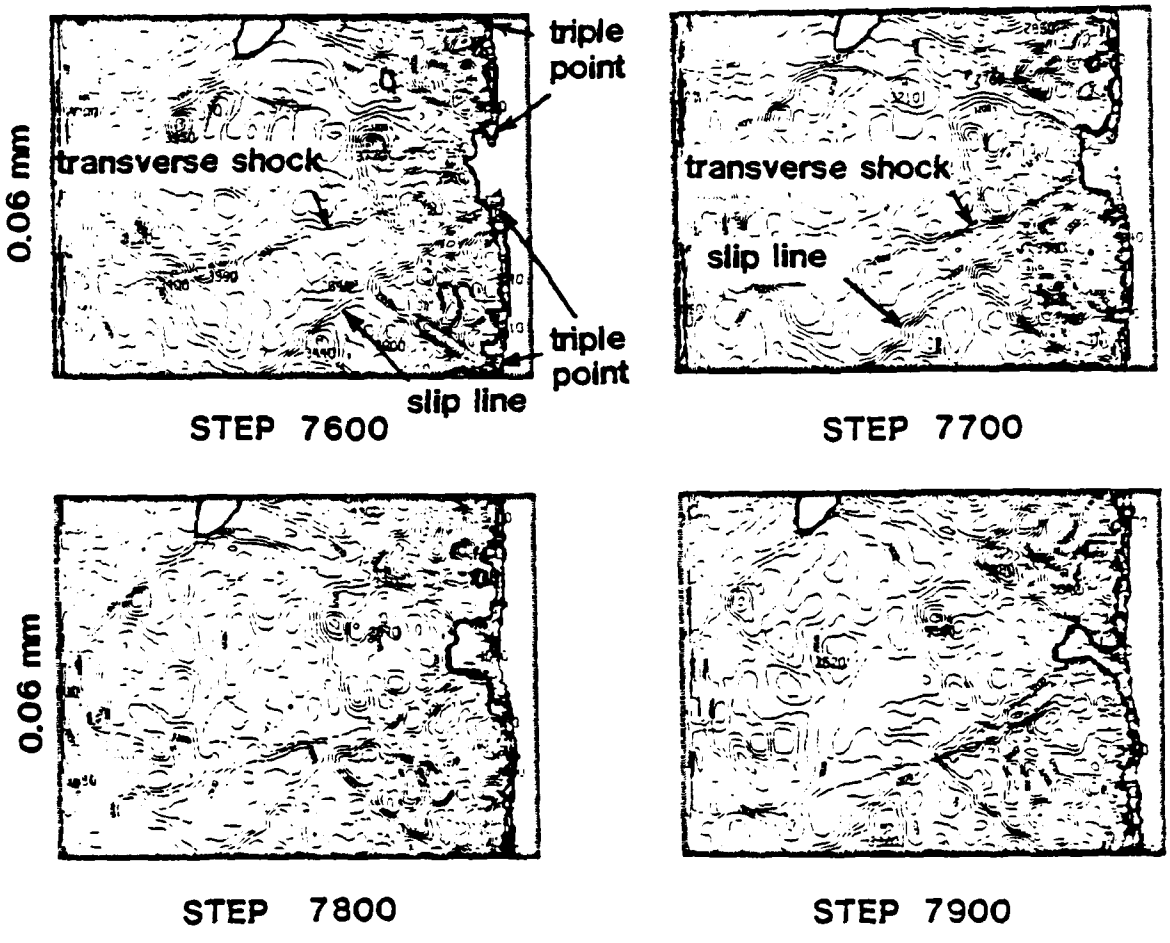

(b)

Fig. 4 (Continued) — Temperature contours behind the detonation wave in Fig. 2. The induction zone is the region in between the leading shock front and the reaction front. (a) Two main triple points divide the channel width; (b) Four main triple points divide the channel width.

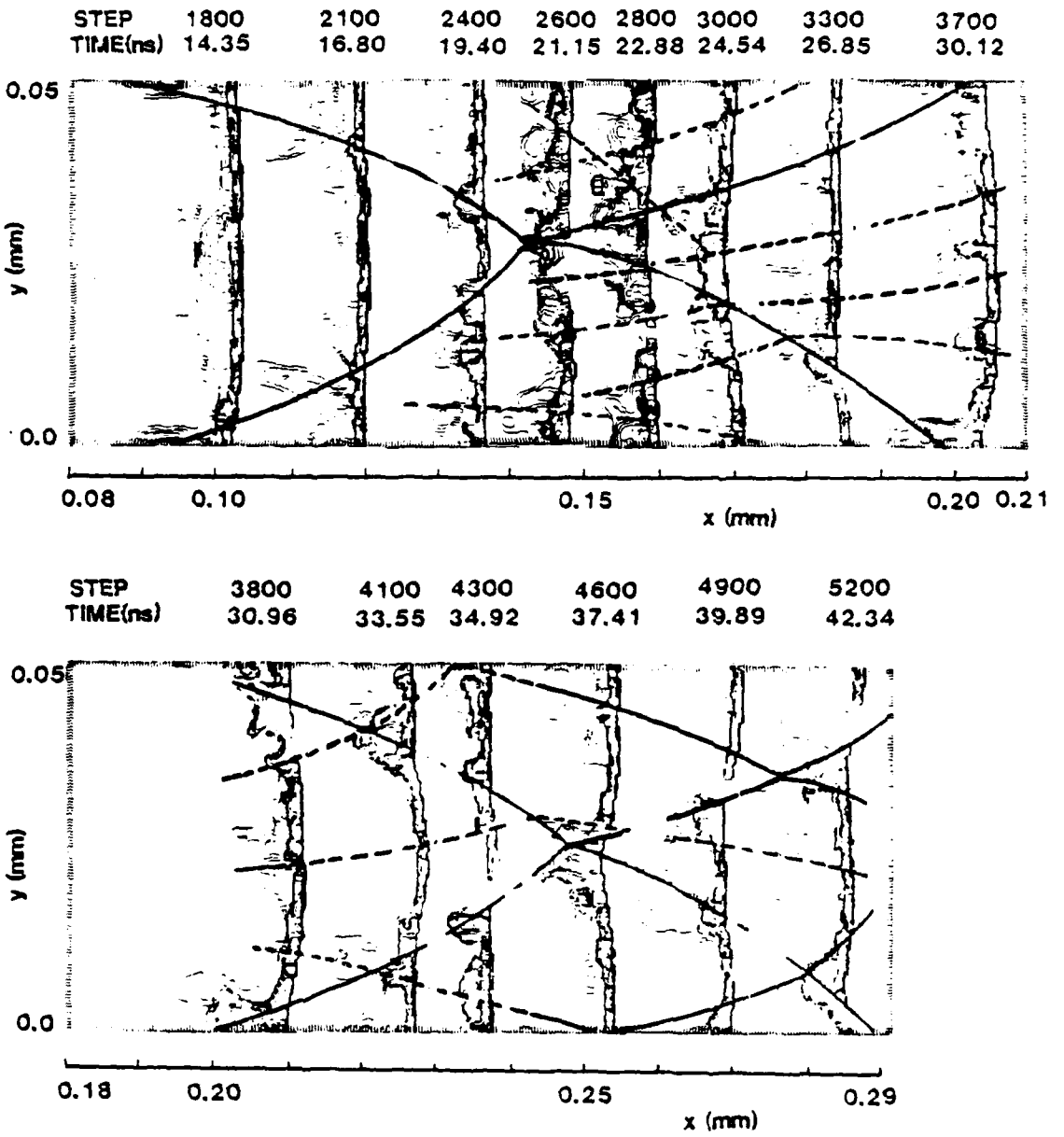

Fig. 5 — Pressure contours of a detonation wave propagating in a channel 0.05 mm wide. Solid traces are loci of main triple points. Dashed traces are loci of secondary triple points.

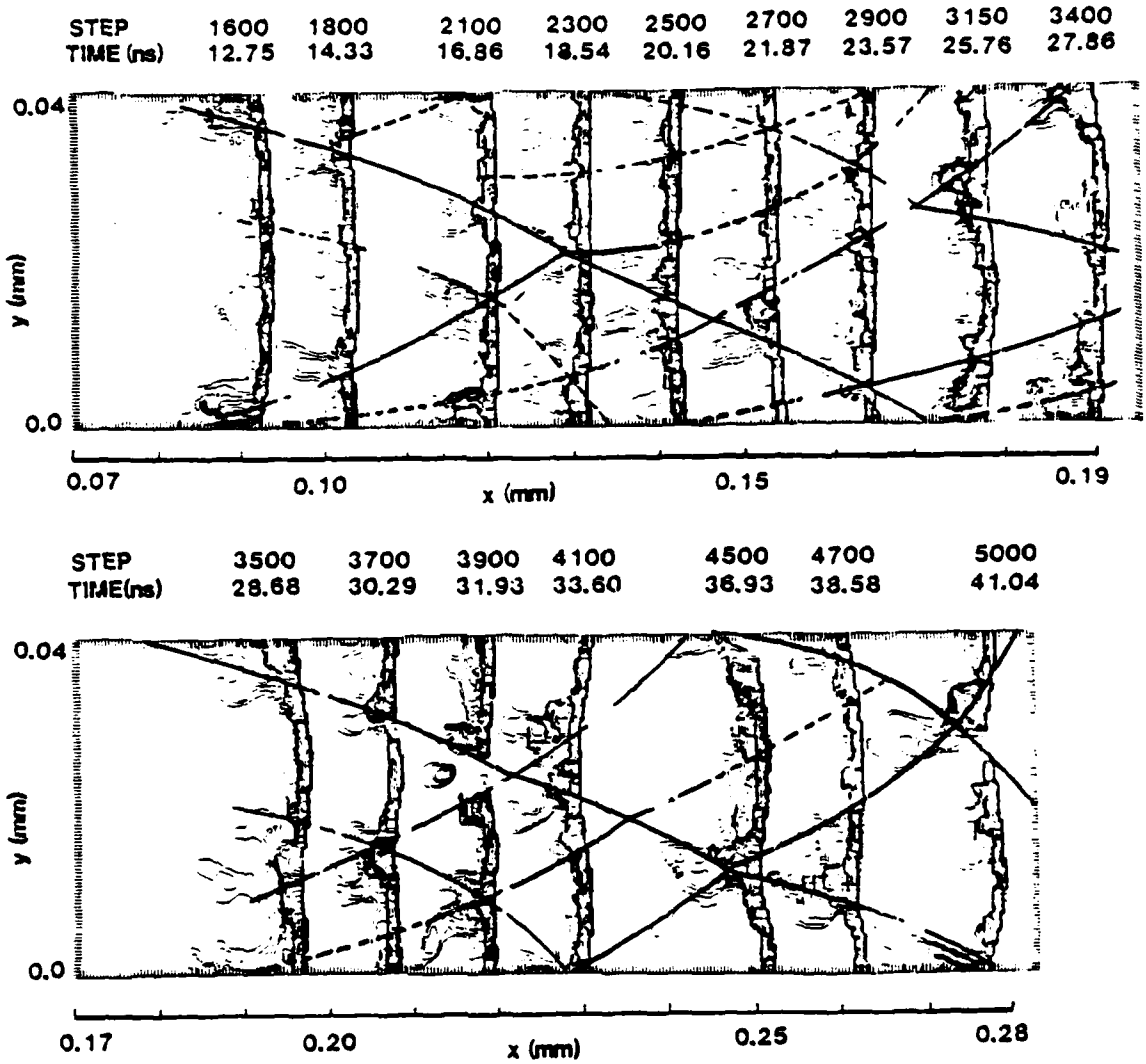

Fig. 6 — Pressure contours of a detonation wave propagating in a channel 0.04 mm wide. Solid traces are loci of main triple points. Dashed traces are loci of secondary triple points.

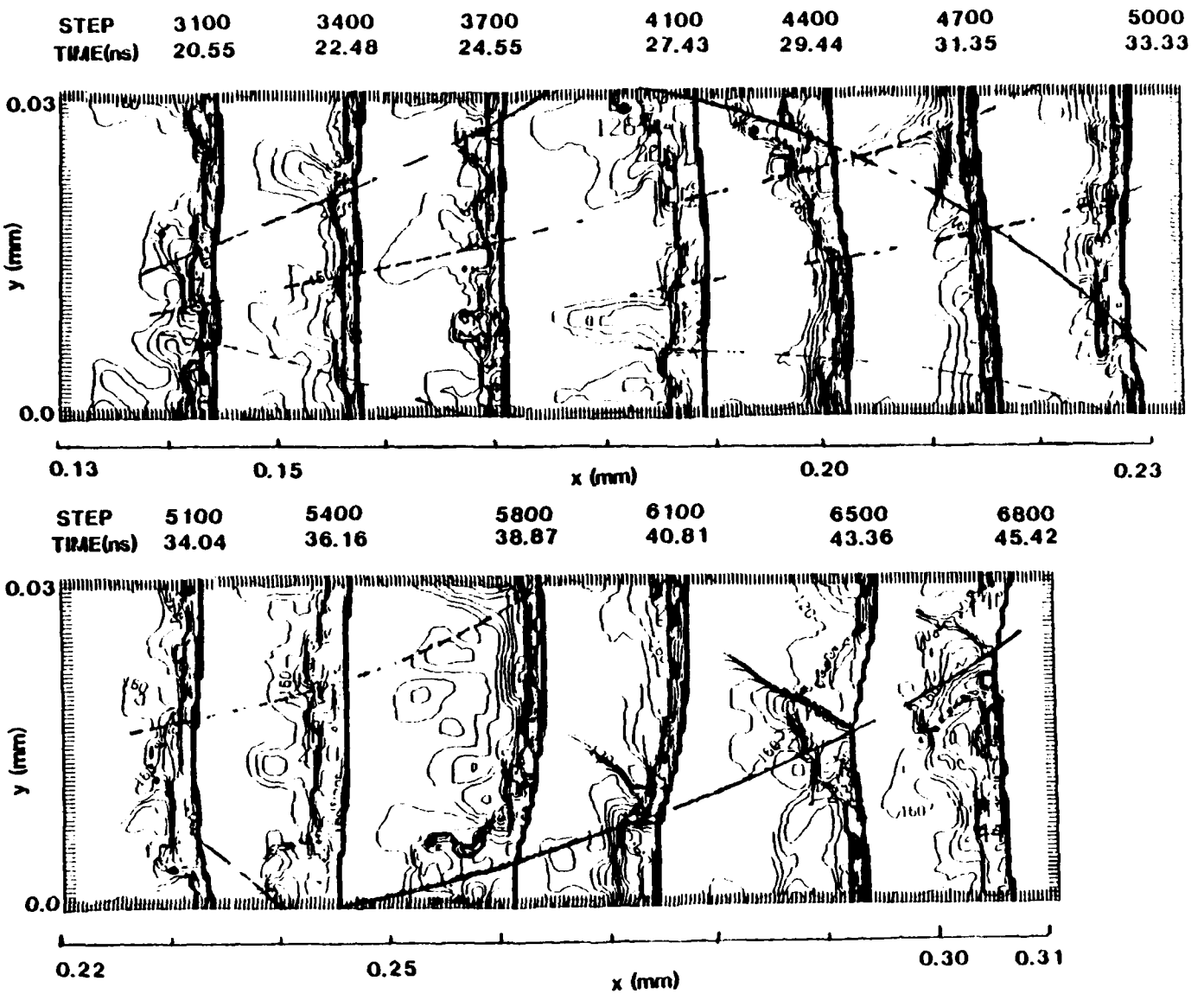

Fig. 7 — Pressure contours of a detonation wave propagating in a channel 0.03 mm wide. Solid traces are loci of main triple points. Dashed traces are loci of secondary triple points.

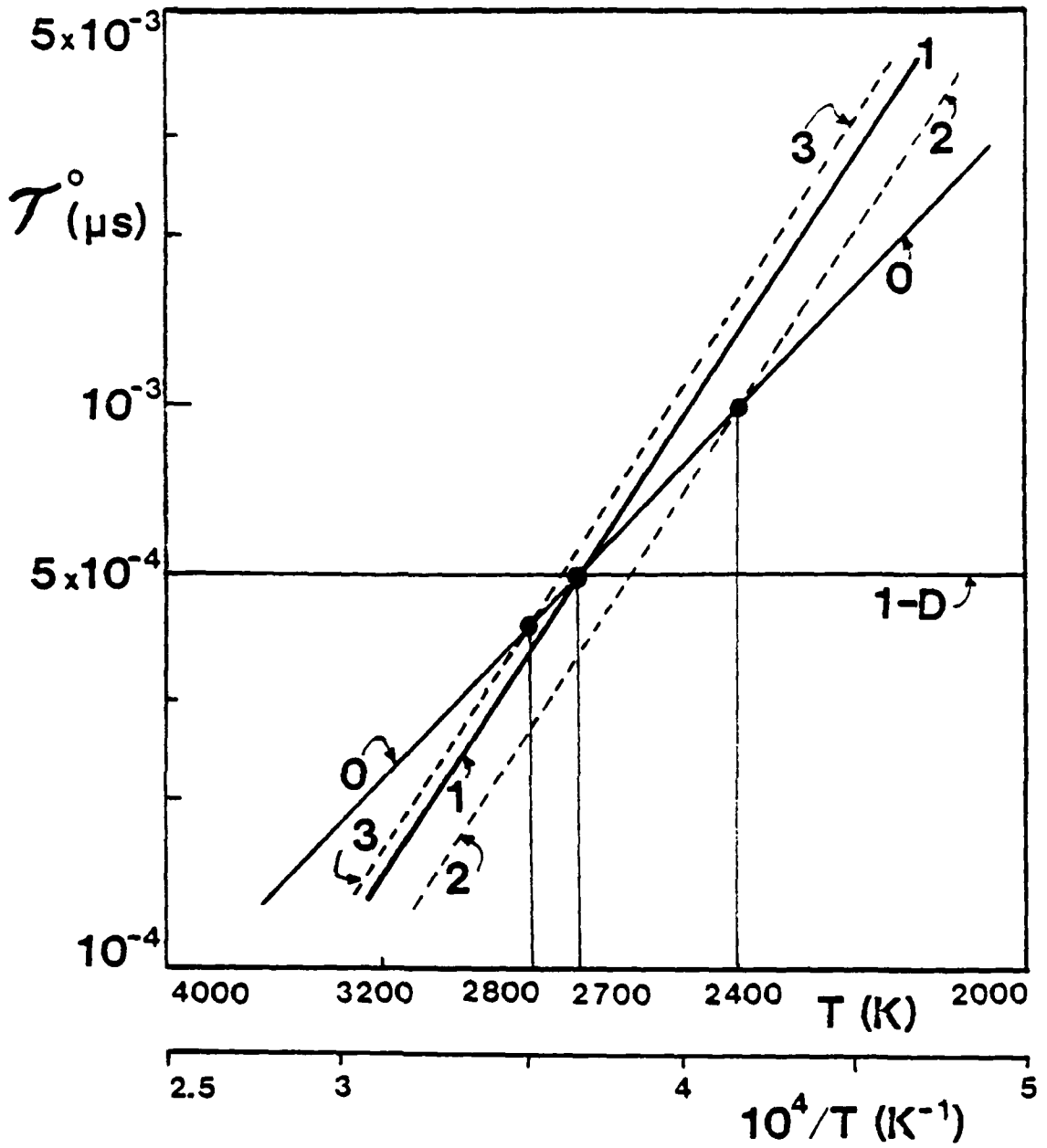

Fig. 8 — Arrhenius plot of induction times versus temperature: $\tau^\circ = A^\circ \exp(E^\circ/RT)$. Line 0, based on experimental data: $A^\circ = 2.3 \times 10^{-6}$ μs; $E^\circ = 29.1$ Kcal. Slopes of lines 1, 2, and 3 are 50% larger than the slope of line 0. For lines 1, 2, and 3, $E^\circ = 43.65$ Kcal.
Line 1, obtained by rotating line 0 about 2700 K: $A^\circ = 1.55 \times 10^{-7}$ μs.
Line 2, obtained by rotating line 0 about 2400 K: $A^\circ = 1.11 \times 10^{-7}$ μs.
Line 3, obtained by rotating line 0 about 2800 K: $A^\circ = 1.71 \times 10^{-7}$ μs.

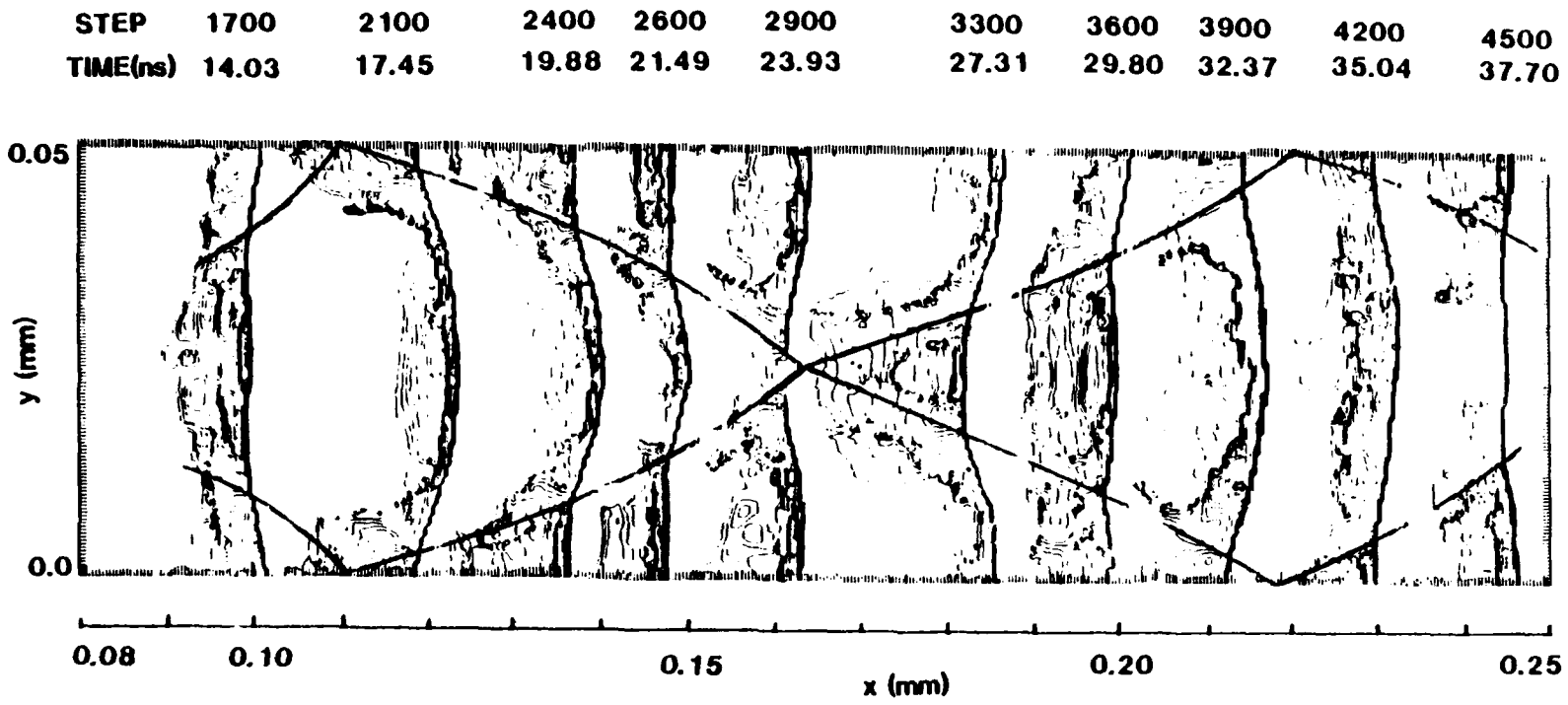

Fig. 9 — Pressure contours of a detonation wave propagating in a channel 0.05 mm wide. Induction time corresponds to line 1 in Fig. 8, obtained by rotating line 0 about 2700 K to a 50% larger slope; $\tau^{\circ} = 1.55 \times 10^{-7} \exp(43650/RT)$ μs. Solid traces are loci of main triple points.

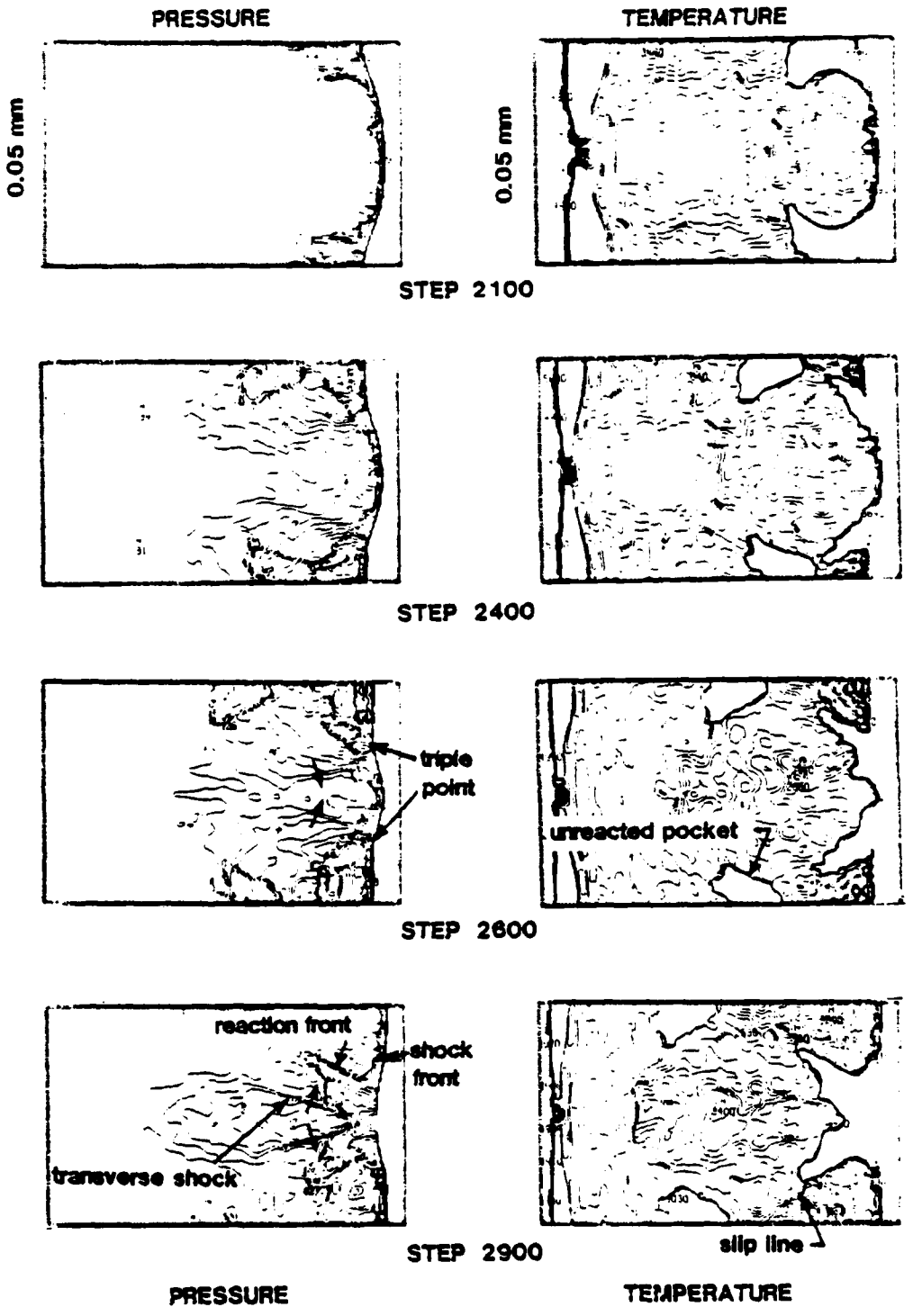

(a)

Fig. 10 — Pressure and temperature contours behind the detonation wave in Fig. 9. (a) Collision of the two triple points at the center of channel; (b) Collision of the two triple points with the walls.

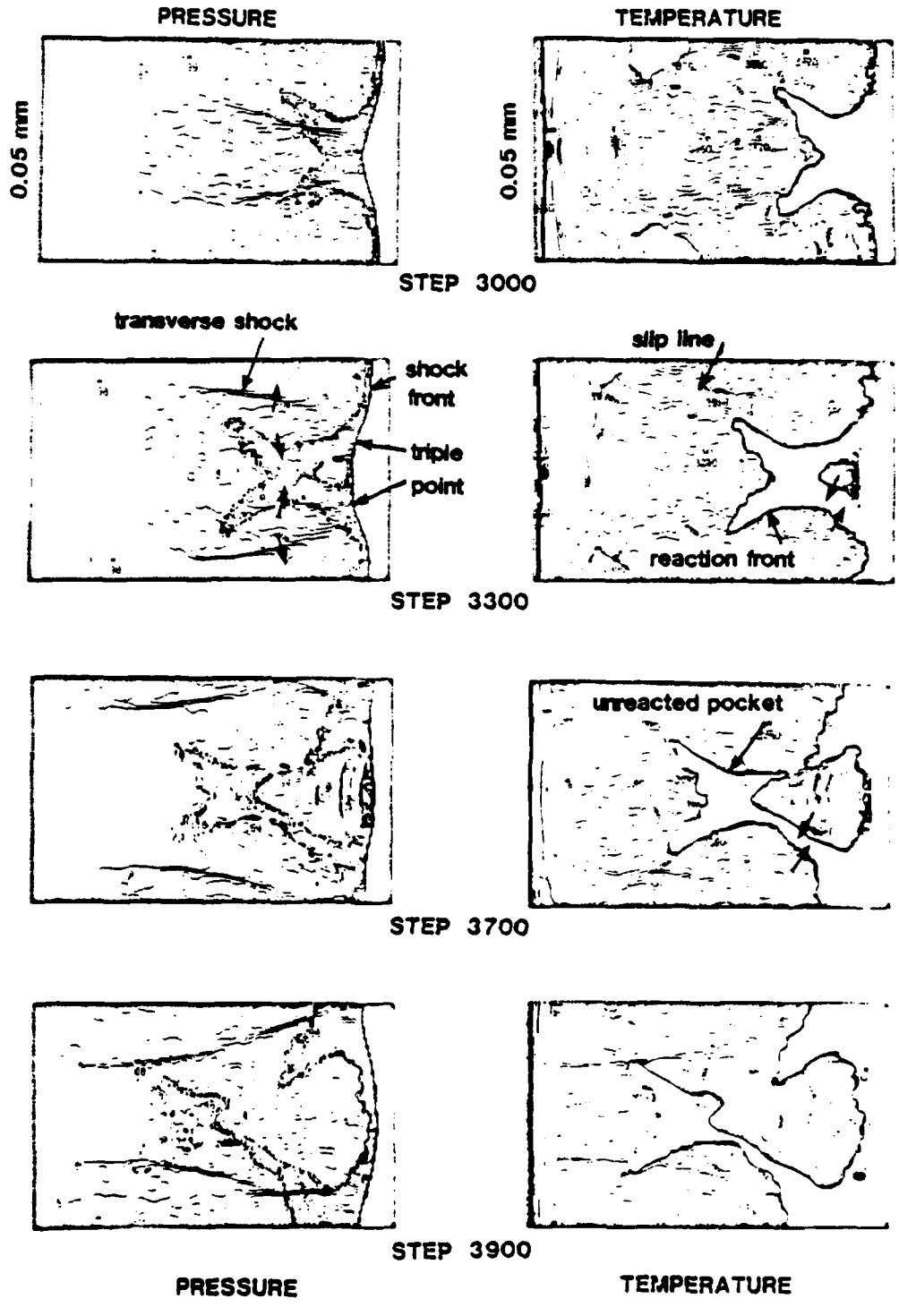

(b)

Fig. 10 (Continued) — Pressure and temperature contours behind the detonation wave in Fig. 9. (a) Collision of the two triple points at the center of channel; (b) Collision of the two triple points with the walls.

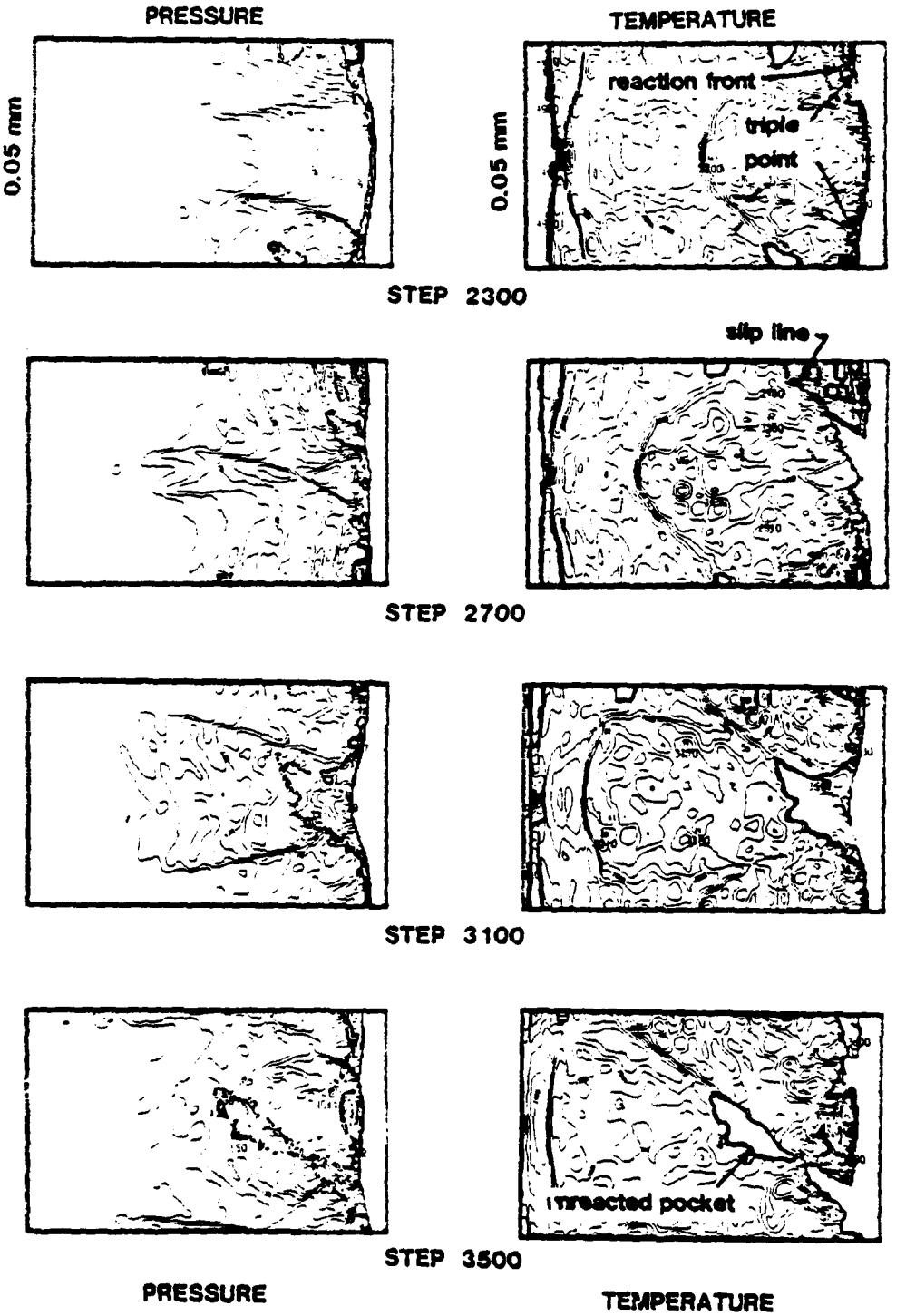

Fig. 11 — Pressure and temperature contours behind a detonation wave propagating in a channel 0.05 mm wide. Induction time is obtained by rotating line 0 in Fig. 8 about 2700 K to a 20% larger slope: $\tau = 7.83 \times 10^{-7} \exp(34920/RT)$ μs.

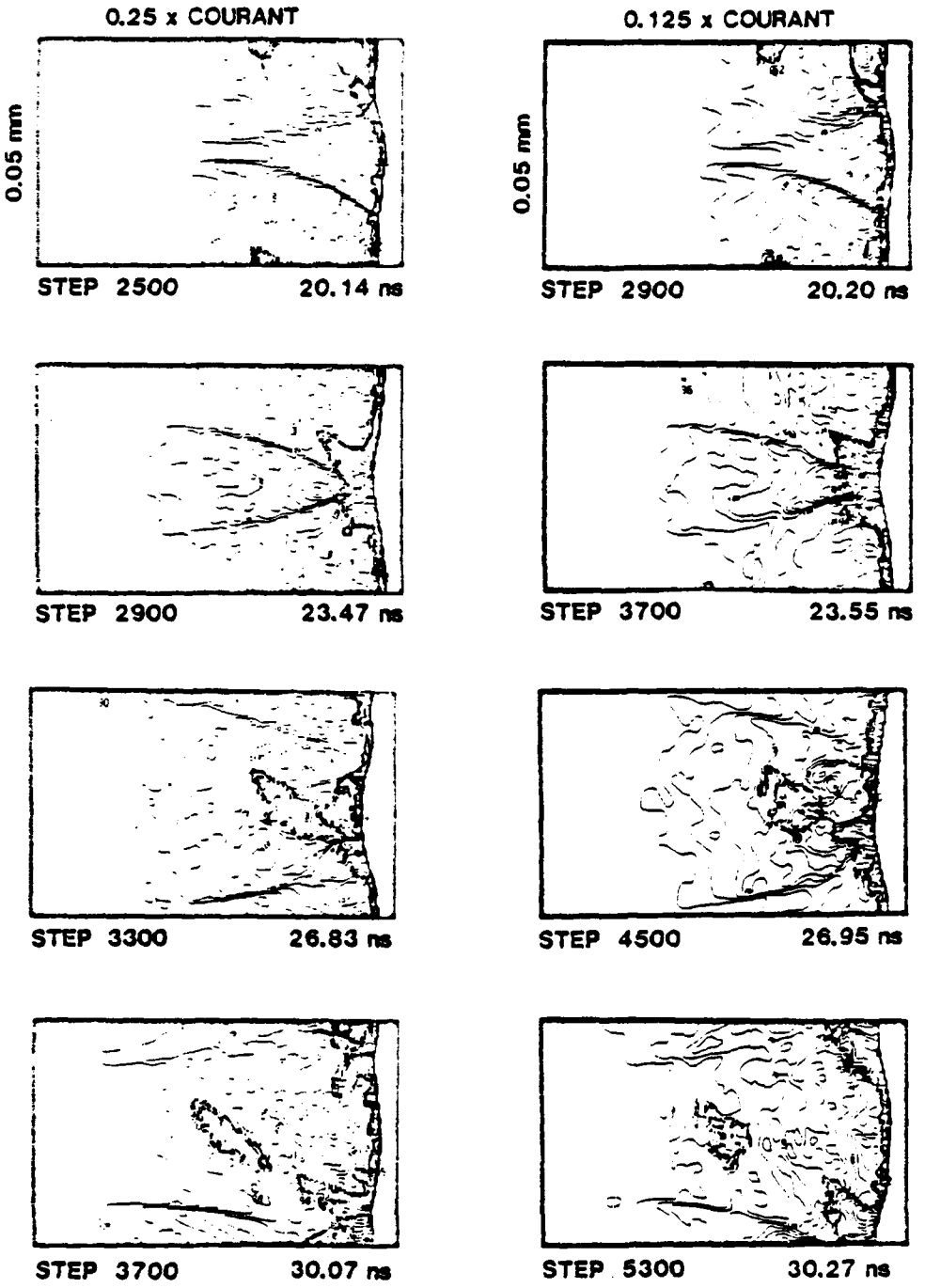

(a)

Fig. 12 — Numerical convergence test for the same conditions of Fig. 11, except that calculation on the right start at step 2100 using a time step half of that used in calculating the results on the left. Comparisons are at nearly equal times, given at the bottom right of each frame. (a) Pressure contours; (b) Temperature contours.

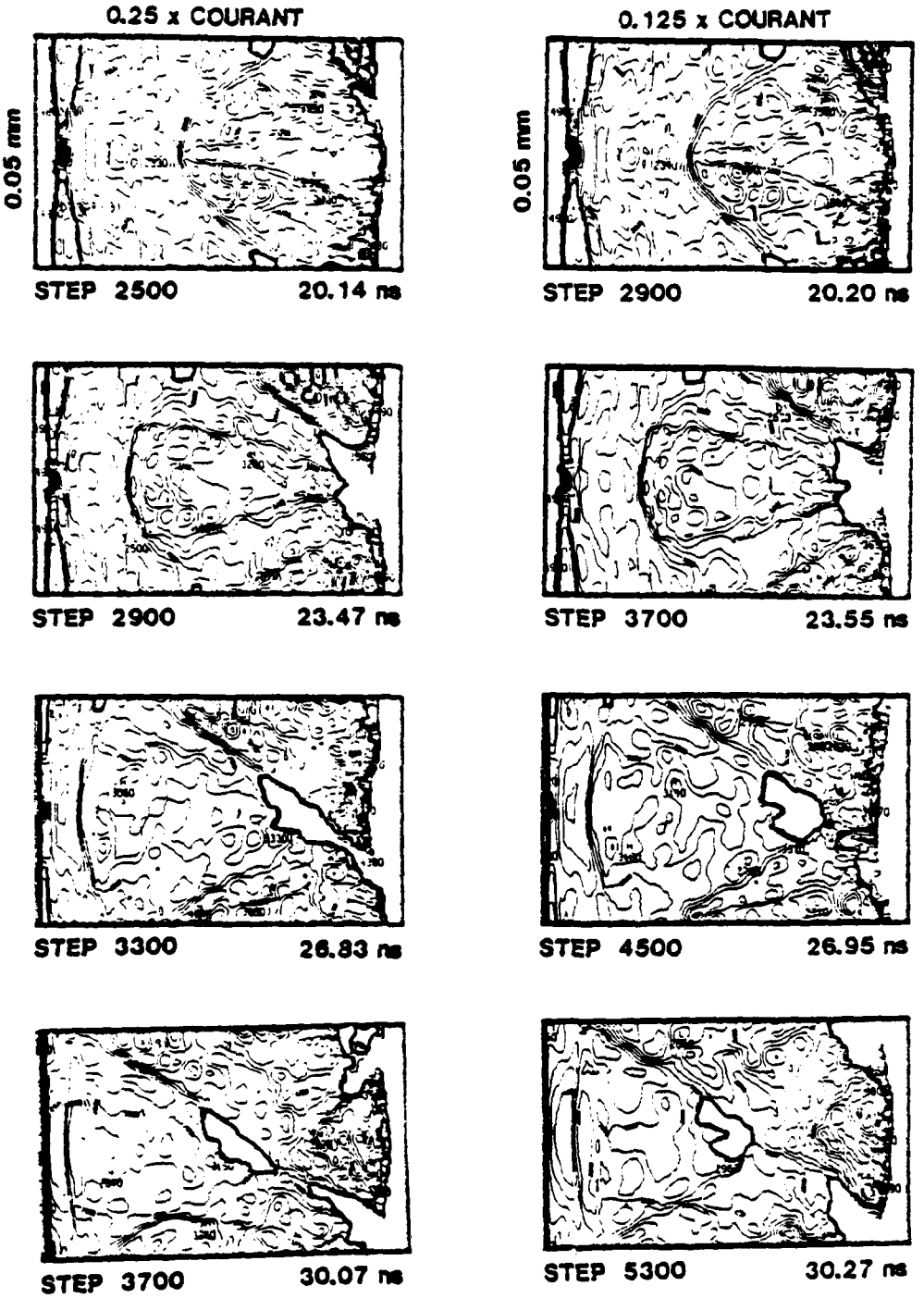

(b)

Fig. 12 (Continued) — Numerical convergence test for the same conditions of Fig. 11, except that calculation on the right start at step 2100 using a time step half of that used in calculating the results on the left. Comparisons are at nearly equal times, given at the bottom right of each frame. (a) Pressure contours; (b) Temperature contours.

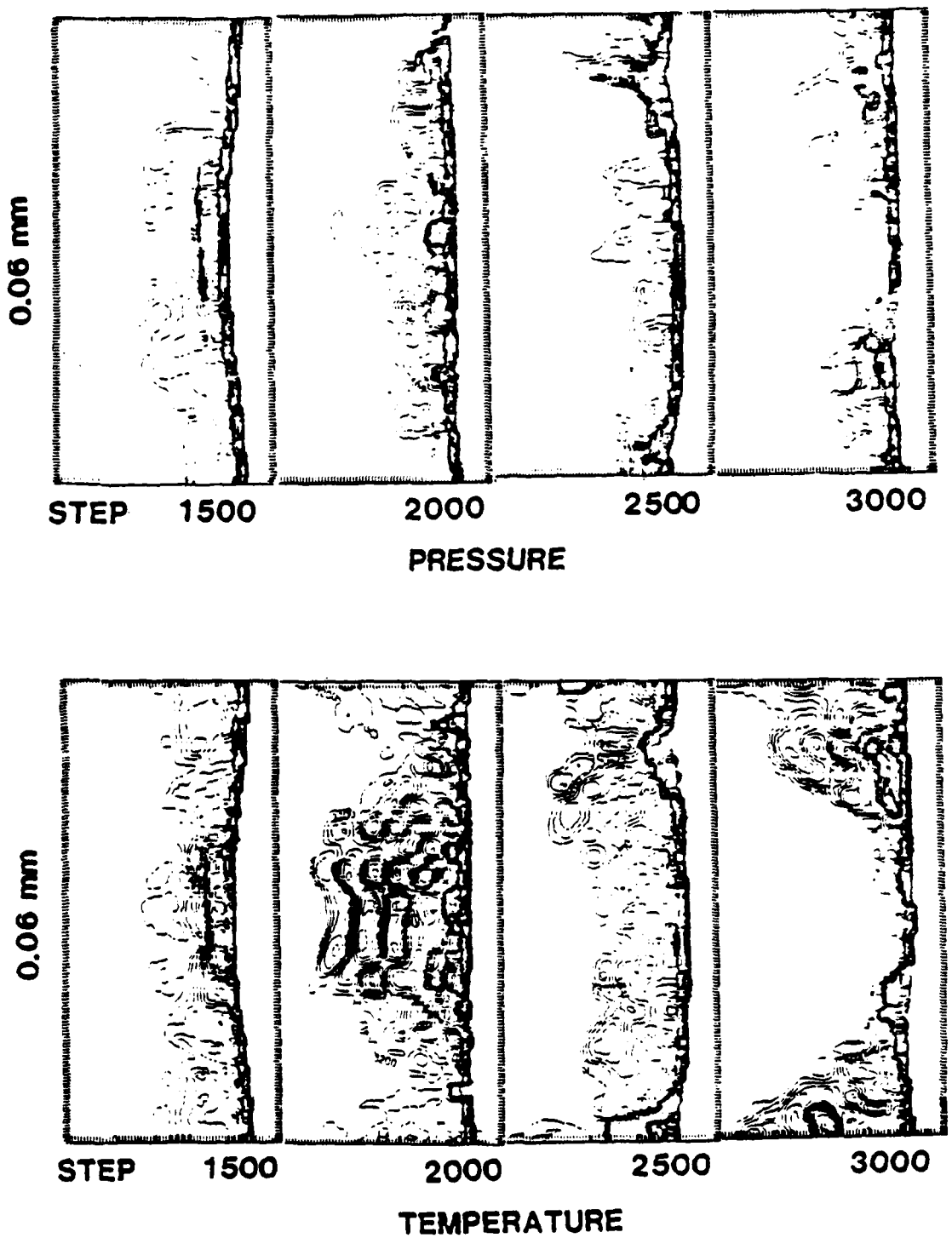

Fig. 13 — Pressure and temperature contours behind a detonation wave propagating in a channel 0.06 mm wide. Induction time corresponds to line 2 in Fig. 8, obtained by rotating line 0 about 2400 K to a 50% larger slope; $\tau^{\circ} = 1.11 \times 10^{-7} \exp(43650/RT)$ μs.

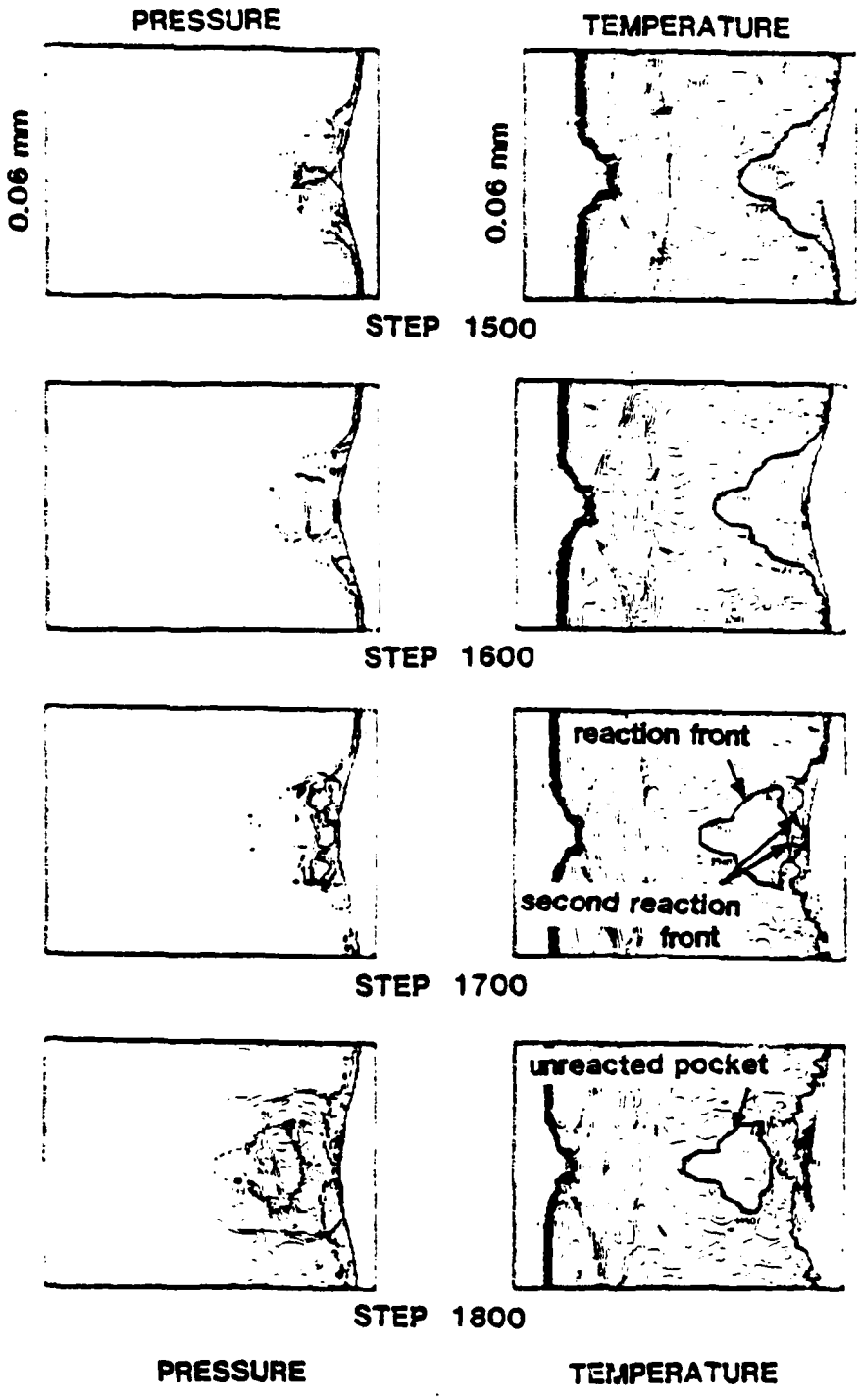

(a)

Fig. 14 — Pressure and temperature contours behind a detonation wave propagating in a channel 0.06 mm wide. Induction time corresponds to line 3 in Fig. 8, obtained by rotating line 0 about 2800 K to a 50% larger slope; $\tau^{\circ} = 1.71 \times 10^{-7} \exp(43650/RT)$ μs. (a) Formation of a pocket of unreacted material at the center of channel; (b) Distortion of structure due to formation of large pockets of unreacted material.

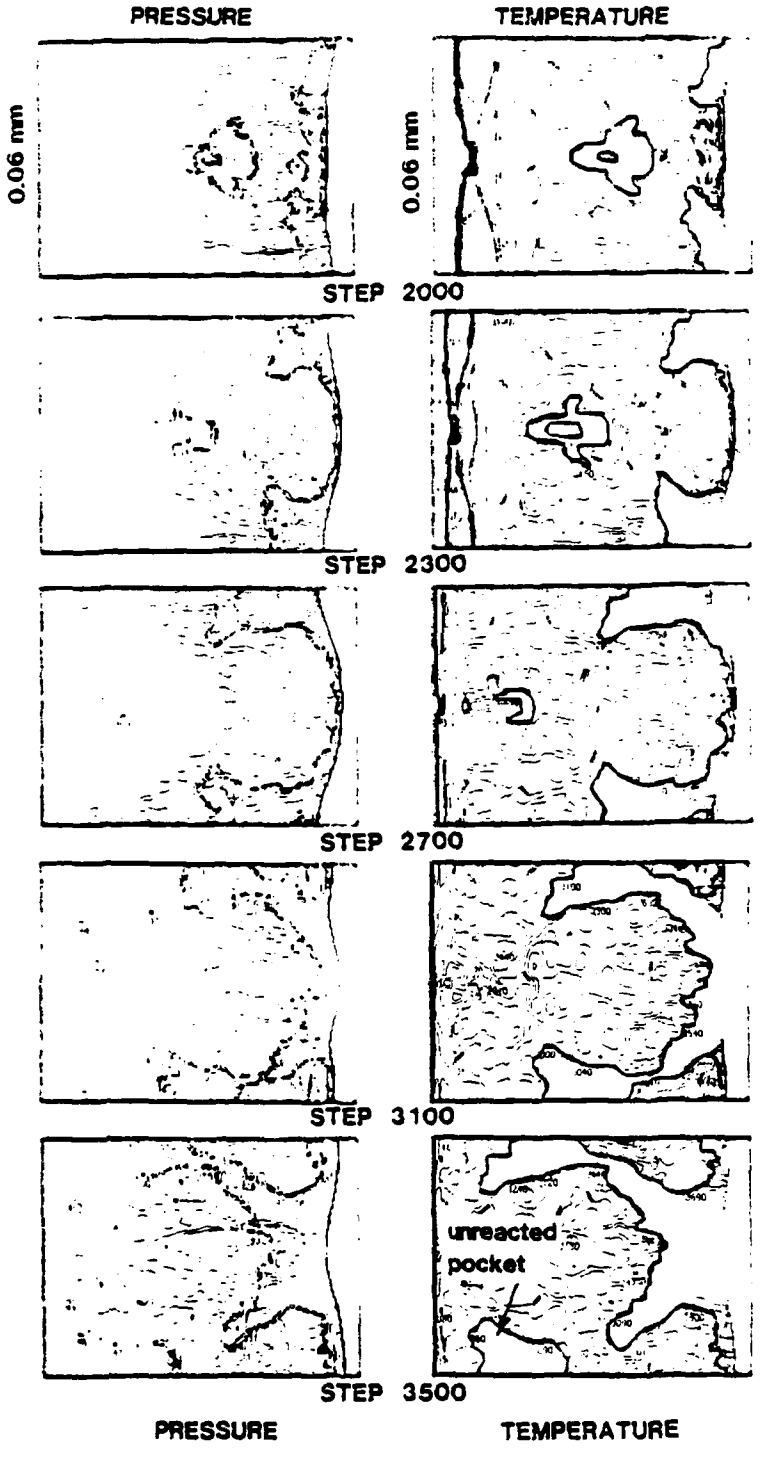

(b)

Fig. 14 (Continued) — Pressure and temperature contours behind a detonation wave propagating in a channel 0.06 mm wide. Induction time corresponds to line 3 in Fig. 8, obtained by rotating line 0 about 2800 K to a 50% larger slope; $\tau^* = 1.71 \times 10^{-7} \exp(43650/RT)$ μs. (a) Formation of a pocket of unreacted material at the center of channel; (b) Distortion of structure due to formation of large pockets of unreacted material.

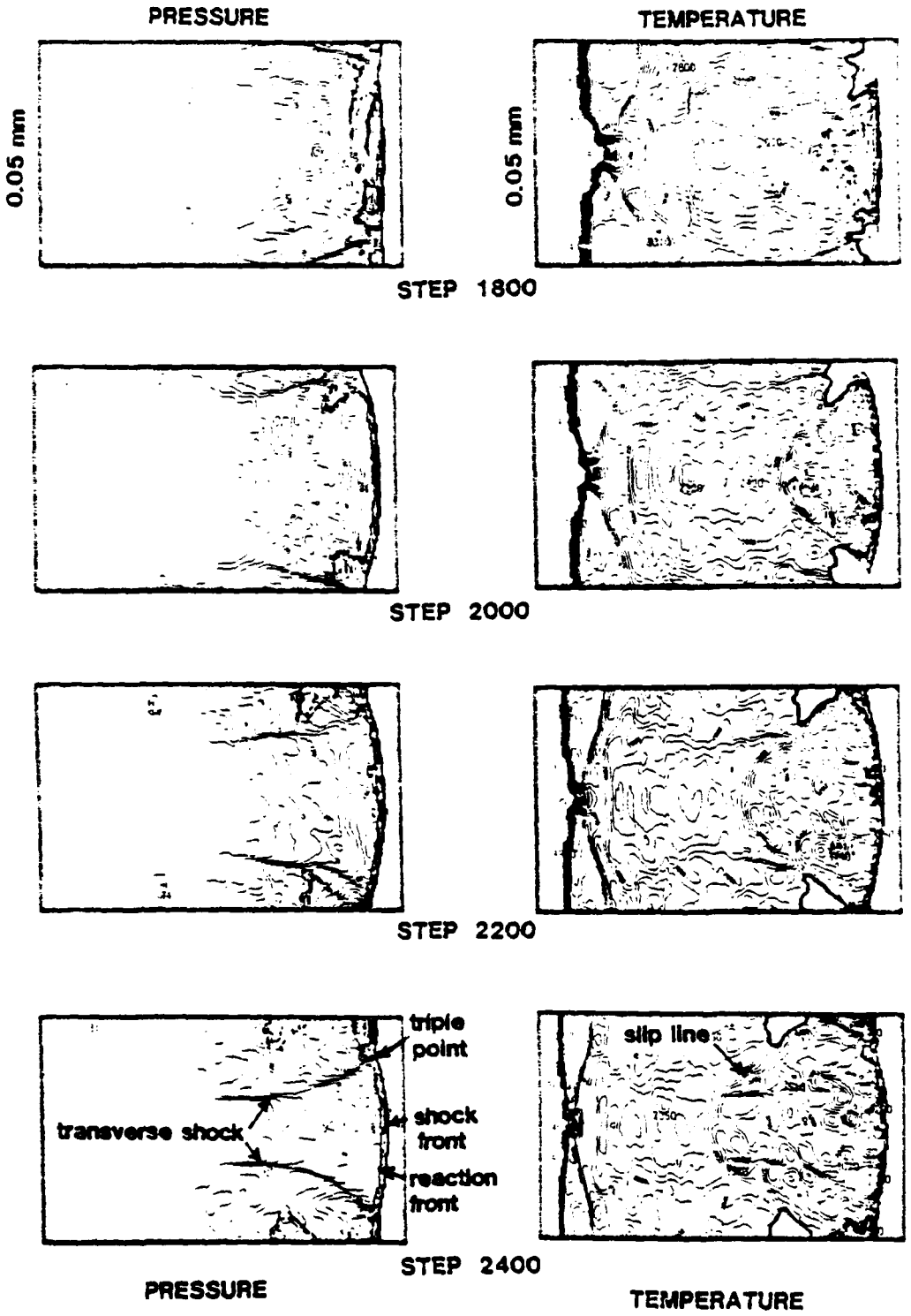

(a)

Fig. 15 — Pressure and temperature contours behind a detonation wave propagating in a channel 0.05 mm wide. Induction time is obtained by rotating line 0 in Fig. 8 about 2700 K to a 30% larger slope: $\tau^\circ = 4.57 \times 10^{-7} \exp(37830/RT)$ μs. (a) Collision of the two triple points with the walls; (b) Collision of the two triple points at the center of channel.

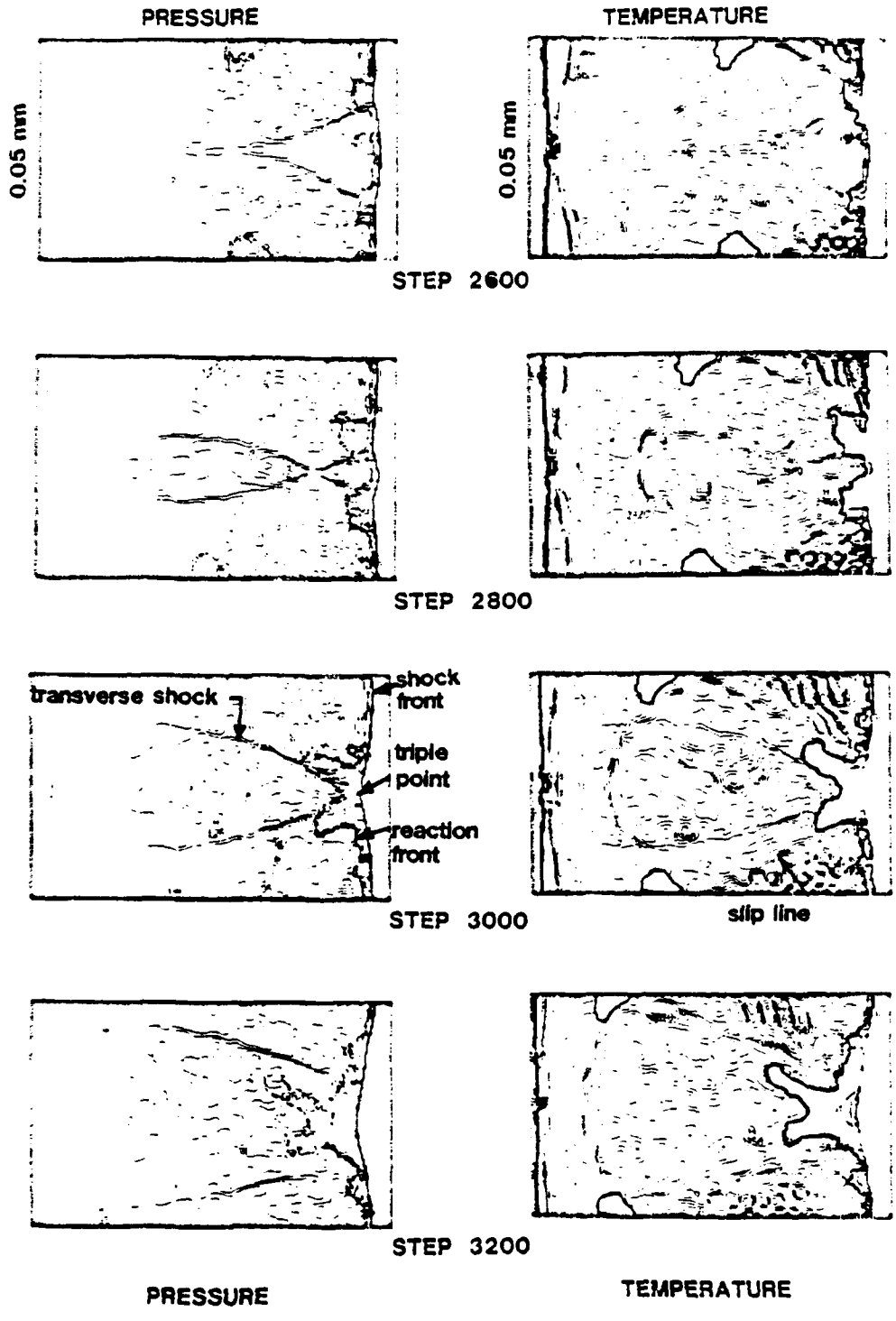

(b)

Fig. 15 (Continued) — Pressure and temperature contours behind a detonation wave propagating in a channel 0.05 mm wide. Induction time is obtained by rotating line 0 in Fig. 8 about 2700 K to a 30% larger slope; $\tau' = 4.57 \times 10^{-7} \exp(37830/RT)$ μs. (a) Collision of the two triple points with the walls; (b) Collision of the two triple points at the center of channel.

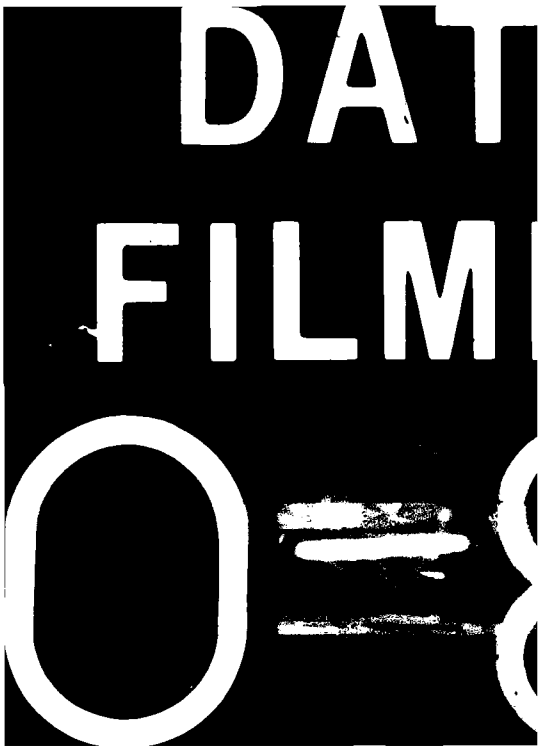
DAT
FILM